Multi-stage metamorphism recorded in crustal xenoliths from Permian dykes of the region of Mrirt (Moroccan Central Massif)

Stéphanie Duchene, Jean-Luc Severac, Nadège Samalens, Youssef Driouch, Ahmed Ntarmouchant, Leo Kriegsman, Mohamed Dahire, Pierre Debat, Sophie Gouy

Multi-stage metamorphism recorded in crustal xenoliths from Permian dykes of the region of Mrirt (Moroccan Central Massif)

List of authors*

Stéphanie Duchene [1]*, Jean-Luc Severac[1], Nadège Samalens[1], Youssef Driouch[2], Ahmed Ntarmouchant[2], Leo Kriegsman[3], Mohamed Dahire[2], Pierre Debat[1], Sophie Gouy[1]

Affiliations

[1] Université de Toulouse, GET, UMR 5563, OMP, CNRS, IRD, 14, avenue Edouard-Belin, 31400, Toulouse, France

[2] Département de Géologie, Laboratoire GERA, Université Mohamed Ben Abdellah, Faculté des Sciences Dhar El Mahraz, B.P. 1796, Fès-Atlas, Fès, Morocco

[3] Naturalis Biodiversity Center, Research & Education Division, Dept. T&S, Darwinweg 2, NL-2333 CR Leiden, Netherlands

(*corresponding author e-mail: stephanie.duchene@get.omp.eu)

Abstract

The Permian magmatic rocks from Morocco contain crustal xenoliths that sample the Variscan crust in a context of widespread magmatism. A series of such xenoliths was collected in Permian dykes of the Central Massif, in the region of Mrirt. The metapelitic xenoliths are silica poor to intermediate ($44<SiO_2<57$ wt.%) and alumina-rich ($17<Al_2O_3<34$ wt.%) and are notably enriched in some HFSE (Nb, Ta, Ti) and some transition elements (Cr, V, W, Ni). Their petrographic evolution depicts a multi-stage evolution from an early, subsolidus, metamorphic history related to regional metamorphism, of which biotite, garnet and sillimanite are the witnesses toward a late thermal evolution coeval with the entrapment in the magma, marked by pervasive partial melting and development of peritectic spinel and cordierite together with K-feldspar and ilmenite. The overall presence of corundum, which relates to the high Al_2O_3 content, accounts for an initial stage of partial melting and magma escape, prior to the entrapment in the magma. Textural and chemical observation suggests further xenolith digestion and melt flux from the xenoliths toward the magma during ascent. Thermodynamic modelling allowing the determination of the pressure-temperature history of each xenolith shows that the initial pressure varies from *ca.* 1.5 to *ca.* 6 kbar, which, considering lithostatic pressure, corresponds to sampling depths of *ca.* 5 to 25 km. The temperatures recorded by the parageneses coeval with partial melting in the presence of spinel are in the range 800-900 °C whatever the pressure, which accounts for rapid heating due to thermal equilibration with the magma. U-Th/Pb dating of monazite by EMPA gives a poorly resolved Permian age of 293 ± 25 Ma for metamorphism in the xenoliths, in accordance with the stratigraphic age of the host rock. The pressure conditions are similar to those recorded for regional metamorphism in the other Variscan outcrops in Morocco, namely the Jebilet, the Rehamna and the Aouli-Mibladen granitic complex, while the maximal temperatures are much higher. The xenoliths thus appear as typical of the Late Variscan geological evolution of the deep

crust in the Moroccan Mesetas, where abundant magmatism was responsible for local crustal heating of a crust previously affected by regional metamorphism.

Highlights

- Metapelitic xenoliths sample Moroccan Variscan crust from 5 to 25 km depth
- Xenoliths record a first stage of regional metamorphism
- High-temperature metamorphism at low-pressure is due to xenoliths entrapment in the magma
- EMPA monazite dating confirms the Permian age of the microgranodioritic dykes

Keywords: crustal xenoliths, Moroccan Central Massif, metamorphism, thermal history, thermodynamic modelling, magma-xenolith interactions

1. Introduction

The presence of granulite facies rocks and migmatites in metamorphic rocks formed at middle to lower crustal level in mountain belts accounts for high geothermal gradients (>30°/km). Such gradients cannot be sustained by normal radioactivity in a crust of standard thickness. Their occurrence claims either for an increase of crustal thickness (England and Thompson, 1984), which induces an increase in radioactive heat production, or for additional heat sources associated to orogenic processes. Specifically, the injection in the crust of magmas of mantle origin may explain significant increase of the temperature (*e.g.* Juez-Larré and Ter Voorde, 2009) whereas magma transfer ensures near-isothermal conditions in middle-low crustal level and high gradients at upper crustal levels (Depine *et al.*, 2008). Magmatic and metamorphic rocks that outcrop together in high temperature orogenic crust are invaluable witnesses of crustal heating but prograde metamorphism is often obliterated by later retrogression associated to a long exhumation history in a thermally unstable orogenic crust. By contrast, crustal xenoliths transported to the surface in volcanic rocks have been shown to record the pressure-temperature conditions prevailing in the crust in the very moment of sampling by the magmas, thanks to their rapid ascent toward the surface. A remarkable example is that of the metamorphic xenoliths trapped in Neogene lavas of SE Spain (*e.g*. Cesare, 2000; Acosta-Vigil *et al.*, 2010; Álvarez-Valero and Kriegsman, 2007), that record, from west to east, both crustal thinning (decreasing pressure) and crustal heating (increasing temperature) and image crustal extension and increasing heat flux related to the opening of the Alborán Sea. Nevertheless, xenoliths also undergo strong albeit short heating during their ascent (Álvarez-Valero *et al.*, 2015), possible partial melting and digestion, that may hamper the record of the *PT* conditions prevailing during magma injection in the crust (*e.g*. Díaz-Alvarado *et al.* 2011; Johnson *et al.*, 2011).

The Variscan crust underwent high-temperature, granulite facies metamorphism associated to magmatism in the Ivrea zone in the Alps (Kunz *et al*., 2018; Petri *et al*., 2017), Calabria (Graessner and Schenk, 2001; Fornelli *et al*., 2011; Duchene *et al*., 2013), Corsica (Corsini and Rolland, 2009; Rossi *et al.*, 2015) and Pyrenees (Guitard *et al*., 1995; Siron *et al.*, 2020). In Morocco, there are only limited outcrops of the Variscan median crust, that mainly shows *MP/MT* greenschist to amphibolite facies metamorphism. However, high temperature granulitic

conditions are retrieved from abundant crustal xenoliths sampled both by Permian and Neogene magmatic rocks (Bouloton *et al*., 1991; Bouloton and Gasquet, 1995; Moukadiri and Bouloton, 1998; Ntarmouchant, 2003; Dostal *et al*., 2005; Elabouyi *et al.*, 2019) that appear as a window into the underlying crust. Here we propose to study a set of crustal metapelitic xenoliths trapped in Permian dykes from the Moroccan Central Massif, in the late stages of the Variscan orogeny, in order to decipher the relative contributions to the metamorphic record of i) general metamorphism and ii) heating during magma emplacement. More specifically, through petrographic observation and thermodynamic modelling, we intend to retrieve the petrogenetic evolution of xenoliths, their pressure – temperature evolution from regional metamorphism toward entrapment in the magma during its ascent and explore the intensity of thermal and chemical crustal – melt interaction.

2. Geological context

In Morocco, witnesses of the Variscan belt are exposed in the Mauritanides, in the Anti-Atlas and in the Meseta domain (Fig. 1a) as summarized by Simancas *et al*. (2005, 2009), Hoepffner *et al*. (2005) and Michard *et al*. (2008, 2010). It is believed that these domains represent the former Gondwana passive margin and are the southern termination of the Variscan belt (Simancas *et al*., 2005, 2009; Michard *et al*, 2010; Martínez Catalán *et al.*, 2021). This passive margin was involved into the orogeny when closure of the Rheic ocean eventually led to the collision between Armorica and Gondwana. No remnant of an oceanic suture exists in the Moroccan Variscan belt, so that several models for the orogeny have been proposed, from that of an intracontinental orogeny (Piqué and Michard, 1989) to a subduction –related orogeny due to either south-eastward subduction of the Rheic ocean under the northern margin of Gondwana (Michard *et al*., 2010) or north-westward subduction of an eastern Paleotethyan oceanic domain (Roddaz *et al*., 2002; Stampfli and Borel, 2002) or a succession of both (Martinez Catalán *et al.*, 2021).

The Central Massif is one of the Paleozoic massifs that constitute the Western Meseta domain, west of the Middle Atlas high. It is composed of a sequence from Cambrian to Permian sediments. The study area is located close to the locality of Mrirt (Fig. 1b), close to the Tighza

Massif and is described in detail in Ntarmouchant (2003). The oldest Paleozoic, undifferentiated Cambrian-Ordovician sediments are detrital sandstones and pelites. Silurian sediments are black to purple shales which represent the decollement level for a series of Devono-Carboniferous duplex system (Ben Abbou *et al.*, 2001). The overlying Devonian sediments are intercalations of carbonates and pelites. The detrital Visean-Namurian stratas, progressively turning into continental deposits, are discordant on the Ordovician to Devonian sediments and have been interpreted as syn-tectonic sediments (Ben Abbou *et al*., 2001; Roddaz *et al*., 2002; Accotto *et al.*, 2020) deposited in a foreland basin. Finally, the Hercynian structures are sealed by Upper Stephanian-Autunian continental redbeds that unconformably overlay the Visean-Namurian sediments and are affected by late Hercynian faulting.

Numerous gabbroic and doleritic bodies intrude the Carboniferous sedimentary layers and form vein swarms parallel to the Hercynian structures. Since they are folded together with the Carboniferous sediments, they are considered as late-Visean to Serpukovian in age (Ntarmouchant, 2003). Later magmatism takes the form of microgranitic dykes or granitoid plutons that crosscut the Carboniferous stratas and structures, but are mainly oriented parallel to the schistosity. A final pulse of magmatic activity is represented by microgranodioritic enclave-rich dykes that crosscut the regional schistosity and all granitic bodies. As they do not cross the mesozoic stratas, those dykes are considered as Permo-Triassic in age.

The following chronology of magmatic events can be depicted in the Western Meseta domain. 1) The early magmatic stage, characterized by a bimodal association, is constrained at 358-330 Ma by U-Pb zircon dating in the Jebilet Massif (358-336 Ma, Delchini *et al*. 2018; 331.18-329.67 Ma, Essaifi *et al*., 2003). 2) The emplacement of syn-tectonic granodioritic to granitic bodies is dated by SHRIMP U-Pb dating on magmatic zircons from xenoliths by Dostal *et al*. (2005) at 285-328 Ma and by $^{40}Ar/^{39}Ar$ ages on a syn-tectonic granite and associated contact metamorphism between 280 and 295 Ma. These ages confirm earlier whole-rock Rb/Sr ages by Mrini *et al*. (1992) in the Jebilet massif and in the Oulmès and Ment area in the Central Massif. In the Tichka area, the granitic stocks have been dated by U-Pb on zircon at 295-280 Ma (Rossi *et al.*, 2016). 3) Late to post-tectonic magmatism is generally considered as Permo-Triassic, based on whole-rock Rb-Sr data at 268 ± 6 Ma obtained on the Rehamna by Mrini *et al*. (1992) and

white micas $^{40}Ar/^{39}Ar$ cooling ages (275 Ma) on a post-tectonic pluton from the Rehamna by Chopin *et al.* (2014), whereas U-Pb lower intercept age on a zircon rim from granulitic xenolith obtained by Dostal *et al.* (2005) suggests Jurassic activity at 235 ± 8 Ma. 4) In the Mrit area, a K-Ar age of 286 Ma obtained on a granitic dyke crosscut by microgranodioritic dyke (Cheilletz, 1984) provides an upper age limit, whereas the age for the latest dykes is constrained by Th/Pb on monazite in the associated Pb-Zn-Ag veins located 2 km south of the sampling area at 254 ± 16 Ma (Rossi *et al.*, 2016).

The Paleozoic series of the Moroccan Variscan belt have been metamorphosed under greenschist to amphibolite facies conditions (Michard *et al.*, 2008; 2010). The highest metamorphic conditions are observed along a NE-SW shear zone (the Western Meseta Shear Zone) that crosscut the Central, the Rehamna and the Jebilet massifs (Michard *et al.*, 2008). The syn-tectonic metamorphic *PT* conditions in the Rehamna domain, reaching locally 620 °C, 6 kbar (Wernert *et al.*, 2016), correspond to a *MP/MT* gradient of *ca.* 35°C/km (Aghzer and Arenas, 1995; 1998). Similar temperatures (628 ± 50 °C) are recorded in the Jebilet area (Delchini *et al.* , 2016). In the study area however, metamorphic conditions do not exceed greenschist facies conditions (365 ± 7°C, Lahfid *et al.*, 2019). The age for *MP-MT* metamorphism is constrained by few direct radiometric in the Rehamna by U-Pb dating on monazite and ^{40}Ar-^{39}Ar dating on amphibole and micas (Chopin *et al.*, 2014; Wernert *et al.*, 2016). The microstructural analysis associated to *in situ* dating depicts a multistage metamorphic history, beginning in the late Carboniferous (minimum ^{40}Ar-^{30}Ar age of *ca.* 310 Ma) with a prograde metamorphic phase associated to thickening followed by a syn-convergence exhumation phase at 310-295 Ma and ending in the Permian (292-275 Ma), while late tectonic granites were emplaced. Contact metamorphism related to syn- to post-tectonic magmatism is described in the Rehamna (Michard et al., 2010) and in the Jebilet (Delchini *et al.*, 2016), where maximum temperature reaches 600 °C for maximal pressure of 3 kbar. In the Central Massif, metamorphic aureoles characterized by the presence of andalusite – biotite – K-feldspar association have been described around the syn-tectonic calc-alkaline plutons and the post-tectonic leucogranitic bodies in Zaër, Oulmès and Ment (Boushaba and Cailleux, 1992; Dahmani, 1995), which leads to pressure estimates of 1.3 to 2 kbar and maximal temperatures of 600 °C.

Moreover, metamorphic xenoliths of sedimentary origin and of high metamorphic grade (amphibolite to granulite facies conditions) have been sampled by late- to post-hercynian magmatic bodies. In the Jebilet massif, late-hercynian granodioritic dykes contain both partially molten quartz, feldspar, biotite bearing gneisses and K-feldspar, plagioclase, cordierite, garnet, spinel, aluminosilicate, corundum and ilmenite bearing peraluminous enclaves (Bouloton *et al.,* 1991; Bouloton and Gasquet, 1995). In the quaternary basalts of the Middle Atlas, metasedimentary enclaves are characterized by a quartz-feldspar-sillimanite-garnet association, the rarity of biotite and the development of hercynite and orthopyroxene as a product of incongruent melting in the granulite facies (Moukadiri and Bouloton, 1998; van Hoeflaken, 2011). In the Zaër granitic pluton (a late-hercynian intrusion of the Central Massif), Haïmeur *et al*. (2003) describe a diversity of metapelitic enclaves, generally characterized by the presence of quartz, biotite, feldspar and cordierite. Several types of xenoliths are distinguished based on the presence or absence of aluminosilicate (andalusite partly replaced by fibrous sillimanite) and of corundum, pyroxene and spinel relics. Corresponding *PT* conditions vary from 600-650 °C, 2 to 2.5 kbar for andalusite bearing samples and 690-770 °C, 4 to 5 kbar in the spinel bearing xenoliths from the Zaër pluton (Haïmeur *et al.,* 2003), 750-800 °C, 3.5 to 3.9 kbar in the Jebilet (Bouloton *et al.*, 1991) and up to 900 °C, 9-11 kbar in the recent lavas from Middle Atlas (Moukadiri and Bouloton, 1998). Note also that granulite facies conditions (830-870 °C; 6 kbar) are reported for high-grade migmatites and enclaves associated to mafic to acidic magmatism from the Eastern Meseta domain (Elabouyi *et al*., 2019).

A set of crustal xenoliths has been collected in the locality of Kariane, 2 km east of Mrirt. Two dykes of 1 to 2 meters in thickness intrude the Ordovician metasediments, with a broadly N40 orientation (Ntarmouchant, 2003) and can be followed over a distance of *ca.* 2 km (Fig. 2a). The emplacement depth of these dykes is not constrained. However, dykes of similar petrographic type and stratigraphic age have been shown to crosscut both Variscan plutons and the Paleozoic metasediments in the eastern Moroccan Massif Central (Ntarmouchant, 2003), or the contact metamorphic aureoles in the Tighza district (Rossi *et al.*, 2016) and Oulmès and Ment plutons, for which pressures were estimated at 2 and 1.3 kbar respectively (Dahmani, 1995; Delchini *et al.*, 2016), which converts to depths of 5 to 7.5 km (considering lithostatic pressure and a density

of 2700 kg/m^3). Moreover, metamorphic temperatures of the Paleozoic metasediments and the geothermal gradient prevailing during the Variscan collision have been estimated from RSCM in the Zaian mountains, and indicate depth of burial of 5 to 8.5 km (Lahfid *et al.*, 2019). We consider this as an upper limit for the emplacement depth of the dykes. One of the two dykes of the Kariane locality is of granitic composition and comprises few metasedimentary xenoliths. Only one of those xenoliths has been collected for this study (*2Kar8*). The second dyke is a microgranodioritic dyke which crosscuts the former one and is considered as post-orogenic since it also crosscuts the regional schistosity (Fig. 2b). It comprises numerous granitic and metasedimentary enclaves (metagreywackes and metapelites) (Ntarmouchand, 2003). The metasedimentary enclaves (Fig. 2c and d) are of small size (less than 10 cm), often elongated in shape and are non-oriented with respect to the dyke orientation. They can present or not an internal schistosity and also present a mineralogic variability (*e.g*. presence or not of andalusite). Twenty-one samples of metapelitic xenoliths from the microgranodioritic dyke have been collected at different places along the dyke and studied in thin sections. A representative set of those samples will be described in the following.

3. Methods

Samples collected in the field are centimer size xenoliths (4-10 cm in length) included in their microgranodioritic or microgranitic host rock. Each sample has been prepared in order to separate i) one slice for thin section across the xenolith ii) one fragment (10 – 50 g) of xenolith for whole-rock analysis and iii) in eight samples, one fragment of the host rock (*ca.* 100 g) for whole-rock analysis. Thin sections have been made in the Géosciences environnement Toulouse laboratory (Toulouse, France). Samples selected for whole-rock analyses were crushed with a jaw crusher and pulverized in an agate mill. Five samples have been selected for detailed petrological investigation on the basis of petrographical observation by optical microscopy and SEM.

Petrological studies by SEM and EPMA were carried out at the Géosciences environnement Toulouse laboratory (GET, Université de Toulouse, France). Backscattered electron images as well as EDS maps were obtained using the JEOL JSM 6360 LV Scanning Electron Microscope (SEM) coupled to an energy dispersive spectrometry (EDS) analysis system Bruker Quantax 800

at the GET laboratory. The analytical conditions used were 20 kV for the acceleration voltage, while a tungsten filament was used as the electron source. Semi-quantitative analytical composition were extracted from selected micro-domains in the chemical maps using the Bruker Hypermap software. Electron Probe Micro Analyses (EPMA) were obtained using the CAMECA SX 50 on polished thin sections using a beam current of 20 nA and an acceleration voltage of 15 keV for major elements. Monazites were analysed for U-Th-Pb dating with an accelerating voltage of 15 kV and 300 nA probe current. The age and associated confidence interval were calculated with the Rpackage NileDam (Montel *et al.* 1996; Seydoux-Guillaume *et al*., 2012; Villa-Vialaneix *et al*., 2013). Analysis of the reference crystal MOACYR gave ages of 487 ± 25 Ma, in accordance with the recommended value of 474 ± 1 Ma (Seydoux-Guillaume *et al*., 2002), later revised to 504.3 ± 0.2 Ma (Gasquet *et al.* 2010) and 507.7 ± 1.3 Ma (Gonçalves *et al.*, 2016).

Major elements and trace elements bulk-rock analyses were obtained by ICP-OES and ICP-MS respectively in the Service d'Analyse des Roches et des Minéraux (SARM), Nancy (France), following the analytical procedures described by Carignan *et al*. (2001).

Isochemical phase diagrams (pseudosections) were calculated in order to constrain metamorphic conditions, *i.e.* pressure and temperature range, of the aluminous xenoliths. Mineral equilibrium calculations were made in the NCKFMASHMT (Na_2O–CaO–K_2O–FeO–MgO–Al_2O_3–SiO_2–H_2O–MnO-TiO_2) system using Perple_X 07 software (Connolly, 2005; Connolly, 2009) with the Holland and Powell (1998) database updated in 2002. Except for sample *Ma10*, the composition of the system was fixed at a local scale from SEM EDS maps. One pseudosection at the whole-rock scale has been calculated for sample *Ma10*. We have estimated the water content from *T*-X_{H2O} diagrams by choosing X_{H2O} leading to the best agreement with observed assemblages as described in the petrography section, in particular the low volume of hydrous phases (namely biotite and cordierite). The solid solutions models are: biotite (Tajčmanová *et al*., 2009); chlorite (Holland and Powell, 1998); garnet (Holland and Powell, 1998); melt (Holland and Powell, 2001; White et al., 2001); cordierite (Berman and Aranovich, 1996); plagioclase (Newton *et al*., 1980); K-feldspar (Waldbaum and Thompson, 1968); ilmenite (White *et al*., 2000); spinel (Holland and

Powell, 1998); staurolite (Holland and Powell, 1998) and white mica (Coggon and Holland, 2002). Phase abbreviations are from Whitney and Evans (2010).

4. Petrography

4.1. Xenolith Ma3

Sample *Ma3* (Table 1) is characterized by a foliation underlined by biotite, sillimanite and elongated garnet (Fig. 3a and b, Fig. 4a). Crystals of biotite are sometimes skeletal (Fig. 3a and 4a). Garnet forms elongated corroded crystals included in alkali-feldspar and contains inclusions of ilmenite, biotite and numerous sillimanite needles oriented parallel to the main foliation (Fig. 3a and 4a). Spinel is rimmed by alkali-feldspar and often contains an inner foliation parallel to the main foliation (Fig. 3b). Cordierite appears as large clear invasive crystals in textural equilibrium with feldspar, locally enclosing internal schistosity marked by sillimanite fibers and containing ilmenite grains (Fig. 3a).

Sample *Ma3* thus records a multi-stage metamorphic history. Biotite, sillimanite and garnet are syn-kinematic minerals and constitute an early mineral paragenesis. Garnet and spinel are both contemporaneous to late compared to the foliation, which they both enclose and crosscut in several places. Feldspar and cordierite are post-kinematic minerals. The overgrowth of K-feldspar at alkali feldspar rims (Fig. 4a and g) as well as the presence of interstitial alkali feldspar enclosing euhedral porphyroblasts of spinel (Fig. 3b) suggest they grew from a melt, in equilibrium with cordierite.

4.2. Xenolith Ma10

Euhedral porphyroblasts of andalusite and garnet are dispersed in a matrix composed of feldspar, biotite, spinel and ilmenite (Fig. 3c and d) (Table 1). Andalusite shows a chiastolitic form and appear surrounded by spinel and plagioclase coronas (Fig. 3c and d). In places, andalusite crystals are fractured and filled with the same mineral association as in the matrix (Fig. 3d; Fig. 4c and i). Rare corundum spreads in the matrix or appears enclosed in garnet or andalusite (Fig. 4c and i). Feldspars are either alkali feldspar or plagioclase. Plagioclase is observed at the rim or in the cracks of andalusite crystals (Fig. 4b, c, h and i). Plagioclase forms a continuous strip in contact with broken prisms of andalusite whereas K-rich feldspar is scattered

in the middle of the fracture (Fig. 4c and i). Tiny crystals of orthoclase are included within the corona of cordierite around garnet. Sillimanite crosscuts and partly replaces andalusite (Fig. 3d), locally also clearly crosscutting the feldspar bearing microcracks (not shown). Garnet crystals are rimmed by cordierite and alkali feldspar (Fig. 3d and 4b). Spinel occurs around and within andalusite crystals and as inclusion in feldspar (Fig. 3d).

To conclude, andalusite, garnet, corundum, alkali feldspar, biotite and ilmenite appear as an early mineral association, whereas plagioclase, spinel, sillimanite and cordierite belong to later parageneses. Several lines of evidence account for the presence of a melt. These include i) the presence of feldspar-rich veinlets (Fig. 4c and i), ii) the clear spatial association of feldspar surrounding euhedral porphyroblasts of spinel in the vicinity of aluminosilicate, which is interpreted to record a melting reaction with spinel as peritectic product (*e.g.* Powell & Downes, 1990; Johnson *et al*., 2004; Álvarez-Valero *et al.*, 2007) (Fig. 3d), iii) the zoning pattern in plagioclase, characterized by a outwards decrease of the anorthitic content in the coronas surrounding andalusite crystals and a decrease of the anorthitic content away from the edges in the microfractures, which witnesses fractional growth from a liquid (Fig. 4i). iv) The presence of ternary feldspars (*e.g.* Or_{20}, An_{15}, Ab_{65} (Fig. 5a) which suggest that they formed under partial melting conditions at *ca.* 900°C (Elkins and Grove, 1990).

4.3. Xenoliths Ma6 and Kar2b

Large euhedral fragmented crystals of andalusite are scattered in a fine-grained matrix of plagioclase (Fig. 3e) (Table 1). Andalusite is rimmed by a spinel-plagioclase association (Fig. 3e and f, Fig. 4d). Rare biotite (not shown) is scattered in the matrix. Acicular corundum appears as inclusions within andalusite (Fig. 3f and h; Fig. 4d). Locally, fibers of sillimanite develop upon andalusite (Fig. 3e and h). Large grains of cordierite are observed in the matrix, always separated from andalusite by a spinel-plagioclase association (Fig. 3e).

Thus, corundum and andalusite are considered as early mineral phases, whereas sillimanite, cordierite, plagioclase and spinel belong to later parageneses. The presence of plagioclase-spinel association at andalusite rim and the presence of interstitial anhedral plagioclase enclosing euhedral porphyroblasts of spinel (Fig. 3g) are interpreted as the witnesses of former partial

349 melting reactions including spinel as a peritectic phase (*e.g.* Powell & Downes, 1990; Johnson *et*
350 *al.*, 2004; Álvarez-Valero *et al.*, 2007).
351
352 *4.4. Xenolith Ma5*
353 Grey abundant spinel appears within large prisms of euhedral plagioclase (Fig. 3i and j; Table 1)
354 and scattered in a matrix composed of plagioclase and rare and biotite (Fig. 3l) (Table 1).
355 Corundum forms generally rounded crystals (Fig. 3k and 4f; Fig. 4l). Corroded garnet crystals
356 (Fig. 3l) form isolated relics rimmed by cordierite and enclosing ilmenite. The rounded shape of
357 garnet and corundum and the plagioclase matrix forming in places large euhedral crystals suggest
358 the former presence of melt. Anhedral interstitial cordierite (Fig. 4f) forms around feldspar and
359 some corundum crystals are rimmed by spinel and/or cordierite (Fig. 3k). This is broadly similar
360 to sample *Ma10*, except for the absence of andalusite in sample *Ma5*. However, the former
361 presence of andalusite is suggested by the squared shape of plagioclase-rich domains (Fig. 3i)
362 that can be interpreted as pseudomorphs of andalusite crystals.
363
364 The early mineral paragenesis therefore comprises garnet, corundum, biotite and ilmenite,
365 whereas spinel, cordierite and plagioclase belong to later parageneses. The presence of a former
366 partial melt is indicated by i) the euhedral twinned plagioclase crystals (Fig. 3j), ii) the presence
367 of interstitial anhedral plagioclase and/or alkali feldspar enclosing euhedral porphyroblasts of
368 corundum (Fig. 3j and k), iii) rational crystal faces of felspar crystals and iv) formation of
369 overgrowths of spinel and cordierite on grains adjacent to feldspar (Fig. 3k) (Johnson *et al.*,
370 2010).
371
372 **5. Mineral chemistry**
373 *Feldspars*
374 In xenolith *Ma3*, only alkali-feldspar is present and crystals present chemical zoning (Or
375 62 to 90 mol.%, Table 2, Fig. 5a). Alkali-feldspar domains are formed by Na-rich crystals with
376 interstitial K-rich domains (Fig. 4g). In xenolith *Ma10*, feldspars composition is highly variable
377 from plagioclase (An 35 to 45 mol.%) to alkali feldspar (Or 47 to 92 mol.%) with several
378 intermediate ternary feldspar compositions (Table 2, Fig. 4h and 5a). Feldspar in xenoliths *Ma6*
379 and *Kar2b* is mainly plagioclase (An 26 to 74 mol.% and 15 to 45 mol.% respectively, Table 2,

Fig. 5a) associated with corundum and spinel in replacement of andalusite (Fig. 4j and k). Rare alkali feldspar (Or 57 to 88 mol.%) is also present in sample *Ma6.* In xenolith *Ma5*, feldspar is a homogeneous (Table 2, Fig. 4l and 5a), with An content comprised between 45 and 53 mol.%.

Spinel

Most of crystals of spinel are grey and belong to hercynitic spinel (Table 3). X_{Fe} varies from sample to sample but appears mostly homogeneous in each xenolith. The lowest X_{Fe} (0.57 to 0.64) is observed in xenolith *Ma5*, the highest in xenolith *Ma6* (0.70 to 0.74), whereas it is intermediate in samples *Ma3* (0.67-0.72), *Ma10* (0.63-0.79) and *Kar2b* (0.64-0.69). The ZnO content reaches 0.5 wt.%.

Garnet

Garnet is present in xenoliths *Ma3, Ma10* and *Ma5*. They are almandine-pyrope garnets, with composition ranging from X_{Alm} = 64 to 73 % in *Ma3* and from X_{Alm} = 59 to 67 % in *Ma10* (Table 4). Garnet from *Ma10* is generally spessartine - richer than garnet from *Ma3* (X_{Sps} up to 6 %), with spessartine content presenting typical bell-shaped profile (not shown).

Biotite

Biotite is generally Ti-rich (TiO_2 3 to 7 wt.% in *Ma10* and up to 8 wt.% in *Ma3*) (Table 4, Fig. 5b). The lowest TiO_2 is observed in sample *Ma5* (TiO_2 < 5 wt.%). X_{Mg} varies from 0.45 in *Ma3*, 0.4 to 0.56 in *Ma10* and 0.49 to 0.56 in *Ma5*.

6. Petrological and geochemical relationships between host rocks and xenoliths

6.1. Host rocks and xenolith contacts

The microgranodiorite host rock has a porphyritic texture with phenocrysts of plagioclase, amphibole, biotite and quartz in a fine-grained matrix composed of quartz, plagioclase, K-feldspar and rare biotite (Fig. 6a). In sample *Ma3* (Fig. 6b), the contact is sharp. A few xenocrysts of biotite from the xenolith are nevertheless present in the host rock near the contact, accounting for mechanical exchange between the host magma and the xenolith. In sample *Ma10* (Fig. 6c), the contact is characterized by a two mm large rim along the xenolith limit where abundant

411 pinnite replaces cordierite. In sample *Ma6*, the contact is underlined by the presence of large
412 andalusite crystals broadly similar to those of the core of the xenoliths and preserving spinel
413 relics (Fig. 6d and e). Such andalusite crystals are sometimes fully enclosed in the host rock,
414 featuring mechanical exchange between the host magma and the xenolith. In sample *Ma5* (Fig.
415 6f), the contact is sharp, with a two mm large rim along the xenolith limit. In the rim, the host
416 rock is characterized by reduced crystal size, the lack of phenocrystals, and the absence of biotite.
417
418 *6.2. Geochemistry of host rocks and xenoliths*
419 Major and trace elements have been analyzed in the xenoliths and their host rocks (Table
420 5). Xenoliths have a low to intermediate SiO_2 content of 44 to 57 wt.% (Table 5, Fig. 7a). They
421 are characterized by a high although variable Al_2O_3 content (18-34 wt.%) that reaches very high
422 values (*ca.*> 30 %) in the silica poorer samples. Alkali content is high ($5 < Na_2O+K_2O < 9$ wt.%).
423 Host rocks have a SiO_2 content of 62 to 68 wt.% (Table 5). In the SiO_2-Na_2O+K_2O diagram (Fig.
424 7b, Cox *et al*., 1979), 6 samples fall in the field of quartz diorite. One sample, *2Kar 8*, coming
425 from a different dyke, has the composition of a granite. Compared to the host rock, the xenoliths
426 are enriched in a number of trace elements (Fig. 8a and 9), notably HFSE (Nb, Ti) and some of
427 the transition elements (Cr, V, W, Ni). By contrast, there is no element for which there is a
428 systematic enrichment of the host rock compared to the xenolith.
429
430 Host rocks present very similar decreasing REE spectra, with $(La/Yb)_N$ in the range 13-16 (Fig.
431 8b and 9a). The microgranitic sample *2Kar 8* presents a slight Eu anomaly. Xenolith samples also
432 display decreasing REE spectra, broadly parallel, either above or below the host-rock spectra,
433 with 5 samples presenting $(La/Yb)_N$ values similar to that of the host rock and 4 samples
434 presenting $(La/Yb)_N$ scattered between 5 and 30 (Fig. 8b). Note that the $(La/Yb)_N$ ratio is not
435 correlated to the SiO_2 content of the xenolith. The overall REE content varies by an order of
436 magnitude in the xenoliths, the more enriched samples (*Ma3*, *Ma10*, *Ma5, 2Kar5*, *Kar2b*) having
437 the lowest SiO_2 content (44-51 wt.%). The extended spectra highlight negative anomalies for both
438 the host rocks and the xenoliths in Nb, Ta, Ti and P, and a positive anomaly in Pb. No correlation
439 was found between the chemical composition of the host rock and corresponding xenolith.
440
441 **7. Mineral equilibria modeling**

442

443 *7.1. Ma3 xenolith*

444 A pseudosection has been drawn for the local composition of a microdomain in sample
445 *Ma3* (EDS map Fig. 6a and Fig.10). The microdomain is fully representative of the mineral
446 assemblages at the thin section scale. The mineral assemblage (biotite + melt + plagioclase + K-
447 feldspar + spinel + garnet + sillimanite + ilmenite) is stable in the pseudosection for a
448 temperature range of 850-900°C and for a pressure higher than 5 kbar. Isopleths curves for garnet
449 and biotite are reported in the pseudosection and are in agreement with such *PT* range. They
450 define a narrow range between 850 and 915 °C. Modes at this temperature correspond to K-
451 feldspar 50 wt.%, biotite 10 wt.%, garnet 15wt.%, ilmenite 5 wt.%, melt 10 wt.%, plagioclase
452 <5 wt.%, sillimanite <5 wt.% and spinel 5 wt.%, in agreement with petrographic observations.
453 The fraction of melt calculated at 850-900 °C is estimated as 15-25%. Partial melting may have
454 started at a temperature of *ca.* 725 °C in the stability field of garnet and sillimanite for a pressure
455 above 5 kbar. The presence of cordierite accounts for a decompression below 5 kbar. These
456 characteristics are accounted for by a prograde path at a pressure above 5 kbar from 725 to 850-
457 900 °C, followed by a decompression path toward lower pressure and temperature conditions, as
458 shown in Fig. 10.

459

460 *7.2. Ma10 xenolith*

461 The pseudosection (Fig. 11) for sample *Ma10* has been calculated for whole rock
462 composition (recalculated from Table 5 for a water content of 0.54 wt.% determined from T-X_{H2O}
463 section) since none of the microdomain was representative of the sample. In the pseudosection
464 the mineral assemblage (biotite + cordierite + plagioclase + K-feldspar + garnet + spinel +
465 sillimanite + ilmenite+melt) is reached for temperatures between ~800 to 850 °C and pressures
466 between 4 to 6 kbar. The upper and lower temperatures are constrained by the presence of biotite
467 and spinel in the mineral assemblage respectively, whereas pressure is constrained by the garnet-
468 cordierite stability field. The isopleths for plagioclase, biotite and garnet compositions better
469 constrain the temperature to ~850 °C (Fig. 11). Modes at 850 °C correspond to biotite 15 wt.%,
470 plagioclase 10 wt.%, K-feldspar 20 wt.%, sillimanite 30 wt.%, garnet 10 wt %, cordierite
471 <5 wt.%, spinel <5 wt.%, melt <5 wt% and ilmenite <5 wt.%, and are in agreement with
472 petrographic observations. In addition, the observations of i) corroded garnet grains and

cordierite growth in the presence of biotite and spinel and ii) spinel at andalusite/sillimanite rims (Fig. 3c) indicate a temperature increase above 4 kbar to reach the peak *PT* conditions. Andalusite chiastolite attests for an early metamorphism (*PT* conditions outside of the range of the pseudosection). Sillimanite may have grown at the expense of andalusite during heating. Sillimanite fibers crosscutting the feldspar-rich veins and the modes calculated from the model (Supplemental material 2) suggest as an alternative that cooling may then have produced both crystallization of feldspar from the melt and growth of sillimanite fibers fringing andalusite crystals.

7.3. Ma6 xenolith

The composition of a microdomain (Fig. 4d and j), silica poor and alumina rich, has been used to compute a pseudosection (Fig. 12). It is representative in terms of petrographic characteristics of the sample at the thin section scale. The H_2O content was fixed to be just low enough to account for the absence of biotite at the solidus, in order to match the observations, *i.e.* no biotite on the microdomain and rare biotite at the xenolith scale. In the pseudosection, partial melting takes place above 800 °C thanks to the consumption of K-feldspar and, at low pressure (<3 kbar) produces small amounts of spinel (*e.g.* Fig. 3g) while consuming cordierite (Supplemental material 3). The observed assemblage corresponds to temperatures higher than 900 °C, as constrained by partial melting and the absence of K-feldspar. Modes at 900 °C correspond to plagioclase 30 wt.%, corundum 15 wt.%, cordierite 20 wt.%, melt 10 wt.%, spinel 10 wt.%, K-feldspar 5 wt.%; sillimanite 10 wt.% and ilmenite <0.4 wt.%, in agreement with petrographic observations. Moreover, the presence of andalusite resorbed and rimmed by a spinel – plagioclase association accounts for an initial metamorphic stage at a temperature lower than 700 °C and a pressure lower than 2 kbar. Andalusite then remains in a metastable state, without being replaced by sillimanite in this microdomain. To summarize, sample *Ma6* thus record partial melting at low pressure (< 2 kbar) with a temperature increase from less than 700 °C to more than 900 °C.

7.4. Kar2b xenolith

The composition corresponding to the microdomain of Fig. 4e and k, silica poor and alumina rich, has been used to compute the pseudosection of Fig. 13. The petrographical features are

representative of the sample at the sample scale. The H_2O content was fixed to be just low enough to account for the absence of biotite at the solidus, in order to match the observations, *i.e.* no biotite on the microdomain and rare biotite at the xenolith scale.

The absence of K-feldspar suggests its almost total consumption by partial melting reaction at *ca.* 900 °C, whereas the absence of garnet constraints pressure to below 4 kbar (Fig. 13). At such low pressure, partial melting would produce spinel (Fig. 3h) at the expanse of cordierite (Supplemental material 4). Modes at this *PT* range correspond to plagioclase 45 wt.%, cordierite 10 wt.%, sillimanite 10 wt.%, corundum 10 wt.%, spinel 10 wt.%, melt 15 wt.%, ilmenite <1 wt.%. Moreover, metastable andalusite grains account for an initial temperature below 650 °C, at a pressure that is further constrained by the absence of garnet to below 2 kbar. As a whole, the observations suggest an increase of temperature from *ca.* 650 °C to more than 900 °C, at a pressure lower than 2 kbar. This evolution is fully consistent with the evolution estimated for sample *Ma6*. Cooling may then have produced both crystallization of feldspar from the melt and possibly sillimanite fibers growing on andalusite crystals (Supplemental material 4).

7.5. Ma5 xenolith

A pseudosection (Fig. 14) has been drawn for the local composition of a microdomain in sample *Ma5* (Fig. 4f and l). It differs from the sample at the sample scale in that there is no garnet relict. In the pseudosection, the mineral assemblage (cordierite + plagioclase + spinel + corundum + ilmenite ± biotite) is stable for temperature of higher that 800°C and for pressure lower than 5 kbar. Mineral modes at 850 °C correspond to plagioclase 55 wt.%, cordierite 9 wt.%, spinel 10 wt.%, ilmenite 2 wt.%, K-feldspar 7 wt.%, corundum 1 wt.% and melt 16 wt.%. These proportions are in close agreement with petrographic observations. The petrographic observation of spinel corona surrounding corroded corundum (Fig. 3k) argues for an increase of spinel proportions along with decrease of corundum above a temperature of 800 °C (Supplemental material 5). Although not visible in the microdomain, the presence of garnet relics elsewhere in the xenolith records previous mineral equilibrium at lower temperature and/or higher pressure (650 to 800 °C for pressures in the range 2.5 – 5 kbar).

8. Ages constraints

534 A few small (<10 µm) monazite crystals have been found in xenoliths *Ma3* and *Ma6*. These were
535 too small and rare for LA-ICPMS analyses but U-Pb dating was attempted by the U-Th-Pb
536 chemical dating method by EPMA. The diameter of the interaction volume below the electron
537 beam (4 µm) allowed only 7 analysis to be done in sample *Ma6* and 21 in sample *Ma3*. In sample
538 *Ma6*, individual data give ages lower than 230 Ma that do not define a single population. By
539 contrast, in sample *Ma3*, the analyses, although slightly dispersed, provide an age of
540 293 ± 25 Ma, or, if restricted to a more coherent population of 11 analyses, 304 ± 3 Ma (Fig. 15).
541
542 **9. A petrogenetic model for the crustal xenoliths from the Moroccan Central Massif**
543
544 *9.1. Evidence for prograde multi-stage evolution and partial melting in the xenoliths*

545 Regional metamorphism is best represented in sample *Ma3* where biotite, sillimanite and garnet
546 underline the foliation and indicate pressure above *ca.* 5 kbar. In low pressure xenoliths (*Ma6* and
547 *Kar2b*), euhedral crystals of andalusite, randomly scattered in the matrix, belong to an early
548 paragenesis and may have formed during contact metamorphism prior to the entrapment or at the
549 onset of heating in the dyke.

550 The peak temperature parageneses formed during ongoing partial melting, as shown by i) textural
551 observations, *i.e.* the presence of feldspar-rich veinlets (*e.g.* Fig. 4c) and magmatic textures of
552 feldspar associations (Fig. 3b, g and j), ii) chemical zoning of feldspar which witnesses fractional
553 growth from a liquid (Fig. 4g, k), iii) the presence of ternary feldspar (Fig. 5a) that suggest that
554 they formed under partial melting conditions at *ca.* 900 °C (Elkins and Grove, 1990).

555 In high pressure samples (*Ma3*, *Ma10*, *Ma5*), post-kinematic mineral associations formed during
556 partial melting overprint foliated domains. These include coronas of cordierite +ilmenite + alkali
557 feldspar around garnet (Fig. 3e, Fig. 4b and h) and spinel crystals crosscutting initial foliation
558 (Fig. 3b) or as coronas around andalusite pseudomorphs (Fig. 3i). In low-pressure samples,
559 secondary minerals associated to partial melting include coronas of spinel and plagioclase around
560 and inside andalusite (Fig. 3f, Fig. 4e and k), and secondary sillimanite developed upon
561 porphyroblasts of andalusite (Fig. 3e). The new products (including melt, neoblasts of spinel,

562 cordierite, K-feldspar, ilmenite) formed from the (garnet) - biotite – andalusite (sillimanite)
563 assemblages. (Cesare 2000; Álvarez-Valero et *al.*, 2007; Álvarez-Valero and Waters, 2010).

564 Partial melting reactions relevant to the conditions observed in the xenoliths of the Moroccan
565 Central Massif have been reproduced in experiments designed to reproduce assimilation of
566 metasedimentary xenoliths in a granodioritic magma at lower crustal level (4 kbar) under water
567 undersaturated conditions by Díaz-Alvarado *et al*. (2011). During heating and partial melting,
568 they have shown that the initial parageneses of metapelitic xenoliths have evolved to form
569 cordierite, spinel and K-feldspar. These minerals may be formed according to the well-studied
570 reactions (*e.g.* Bouloton et al., 1991; Vielzeuf and Holloway, 1988; Patiño Douce and Johnson,
571 1991; Johnson *et al.*, 2004; Álvarez-Valero *et al.* 2007) :

572 $$Bt + And/Sil + Qz + Pl = Crd\ (or\ Grt) + Kfs + melt \quad (1)$$

573 $$Grt + And/Sil + Bt + Pl = Spl + Crd + Kfs + melt \quad (2)$$

574 or, in garnet-free samples (Buick et al., 2004) :

575 $$Qz + Bt + Pl + And/Sil = Crd + Spl + melt \quad (3)$$

576 Experiments undertaken at 3 kbar from 700 ° to 1000 °C on water-rich or water-poor metapelites
577 in order to explain contact metamorphism assemblages (Buick *et al*., 2004) also display mineral
578 assemblages and melting reactions relevant to the present study. In water poor samples, partial
579 melting begins slightly below 750 °C while muscovite, quartz, andalusite, biotite and plagioclase
580 remain from the protolith and sillimanite appears as well as new crystals of cordierite, biotite and
581 plagioclase. Spinel appears in the experiments at *ca.* 800 °C and orthopyroxene at 1000 °C. Melt
582 production is progressive with a main production between 800 and 950 °C when melt fraction
583 reaches *ca.* 50 %. An association of spinel + secondary plagioclase surrounding relicts of
584 andalusite is noteworthy above 800 °C. Moreover, this secondary plagioclase appears richer in
585 An, and melt is peraluminous granitic in composition with normative corundum. This evolution
586 can be compared to that of the more silica-rich sample *Ma3*, the others having different, silica-
587 depleted compositions. In sample *Ma3*, the paragenesis (Bt, Grt, Crd, Pl, Kfs, Spl, Ilm and melt)
588 is comparable to those observed in the experiments between 800 and 900 °C, whereas the

589 comparison with the thermodynamic model (Fig. 10) allows to reduce this interval to 850-900 °C
590 for a pressure of *ca.* 5 kbar.

591 The melting reactions can be deciphered by a comparison of textural observation and
592 thermodynamic modeling. For the composition of the microdomain in *Ma3* (Fig. 10), at high
593 pressure (6 kbar), melting begins at *ca.* 750 °C (Fig. 16a) and involves consumption of biotite,
594 plagioclase, quartz and produces low amount of garnet (reaction 1). The appearance of spinel is
595 linked to a second major melt-producing reaction at 900°C involving the consumption of
596 sillimanite and biotite and the production of ilmenite together with spinel. This leads to the
597 observed mineral assemblage in sample *Ma3* if we except late cordierite that appears at the
598 expanse of garnet during decompression and cooling. At lower pressure (2.5 kbar, Fig. 16b),
599 thermodynamic modeling shows that melting reaction begins at lower temperature (*ca.* 680 °C)
600 and produces cordierite instead of garnet. The appearance of spinel as a peritectic phase takes
601 place at *ca.* 850 °C and melt is produced at the expense of biotite, plagioclase, K-feldspar and
602 cordierite. Note also that partial melting leads to the disappearance of quartz at high temperature
603 at 775 to 825 °C depending at low and high pressure respectively. However, for the composition
604 of the microdomain in sample *Ma5* (Fig. 14), melting is slightly different (Fig. 16c). It is shifted
605 to higher temperature (800 °C) and involves a single process of consumption of biotite,
606 plagioclase and cordierite but also corundum and production of spinel, K-feldspar and ilmenite.
607 According to the simulation, the growth of secondary cordierite in low temperature sample *Ma5*
608 and *Kar2b* would not be directly related to partial melting but rather to an earlier solid-state
609 reaction consuming biotite, sillimanite and small amounts of spinel to form cordierite, K-feldspar
610 and corundum.
611

612 *9.2. The significance of corundum and the depleted protolith of the xenoliths*

613 Corundum has been observed in all samples except *Ma3*. These samples are characterized by
614 their poor to intermediate SiO_2 and high Al_2O_3 content (44 to 57 wt.% SiO_2, 17.5 wt.% to
615 33.8 wt.% Al_2O_3). Corundum belongs to the early mineral parageneses since it appears as
616 inclusion in andalusite and garnets. However, it remains euhedral and stable in the late, high
617 temperature parageneses together with feldspar and spinel. Thermodynamic calculations show

618 that the presence of corundum is controlled by the chemical composition rather than by the
619 pressure-temperature conditions. Thus, in the simulations, corundum is absent when SiO_2 is
620 higher than 50 wt.% and Al_2O_3 lower than 30 wt.% (Fig. 10), present over the whole *PT* range
621 when SiO_2 is lower than 40 wt.% and Al_2O_3 higher than 45 wt.% (Fig. 12 and 13) and restricted
622 to limited low-pressure domains (<5 kbar) at high temperature (>600 °C) for intermediate SiO_2
623 and Al_2O_3 contents (Fig. 11 and 14). Reaction textures preserved in spinel–corundum–feldspar-
624 rich rocks show corundum partially replaced by spinel, which is consistent with numerical
625 modelling that shows corundum consumption and spinel production above 800°C (Fig. 16c) and
626 has been already described by Johnson *et al*. (2010). It has been suggested that the presence of
627 corundum is favoured by high H_2O content (Johnson *et al*., 2010). However, according to
628 thermodynamic modelling corresponding to the composition of sample *Ma5* (Fig. 16d), an
629 increase in H_2O content (from 0 to the observed value of 0.56 wt.%) would rather correspond to
630 the disappearance of corundum. At the composition corresponding to the studied microdomain,
631 corundum is present at a pressure of 3kb from 550 °C to 980 °C with a maximum modal
632 abundance of 6% at *ca.* 850 °C.

633

634 *9.3. Magma – xenoliths interactions and the origin of the refractory nature of the xenoliths*

635 There are two lines of evidence for chemical – mechanical magma-xenolith interactions in the
636 samples from the Moroccan Central Massif. The first one is the petrographic observation of some
637 digestion of the xenolith by the enclosing magma. This is marked by the presence of biotite and
638 andalusite xenocrysts in the host rock at the contact with xenoliths in a number of samples (Fig.
639 3b, d and e). The second one is the observation of a linear relationship between the transition
640 element and SiO_2 content in the host rock sampled in the vicinity of the xenoliths, which we
641 tentatively interpret as a witness of chemical mixing between transition element enriched
642 xenoliths and the enclosing magma (Fig. 8a). Such digestion of the xenoliths by the enclosing
643 magma, and partial melting and melt loss due to heating at their contact, has been long observed
644 and taken as a marker of crustal contamination during magma ascent. In particular, this process
645 has been recently addressed on Díaz-Alvarado *et al*. (2011), which explained the shift from calc-
646 alkaline magmas toward peraluminous granite composition by the assimilation of crustal xenolith

647 that underwent partial melting and retained a solid fraction containing in particular the peritectic
648 phases formed by partial melting reactions.
649
650 Such a process requires substantial amount of melt loss, which is difficult to evidence from the
651 chemistry and the mineralogy of the residue. Indeed, as recalled by Johnson *et al*. (2010), melt
652 loss at a given temperature would not change significantly mineral proportion and chemical
653 composition of the residue. Hence, the refractory nature of the xenolith, marked by the abundance
654 of aluminosilicate phases, spinel and corundum, the low SiO_2 and large Al_2O_3 content, must be
655 largely inherited from the protolith. Considering the partition coefficient from Bea *et al*., (1994)
656 relevant for partial melting of crustal material, we have calculated the evolution of the trace
657 element content of the residues for samples *Ma3* (model 1) and *Ma5* (model 2) in the case of non
658 modal batch melting, *i.e.*

659 $$\frac{C_l}{C_0} = \frac{1}{D + F(1-P)}$$

660 where C_l is the concentration of the element of interest in the partial melt, C_0 is the concentration
661 in the initial solid, D is the bulk partition coefficient of the solid and P is the partition coefficient
662 weighted by the proportion that each mineral contributes to the melt. Mineral proportion at the
663 onset of cooling and the proportion of the mineral that contributes to the melt at a final
664 temperature of 900°C are taken from the thermodynamic calculation (Table 6). The two samples
665 represent contrasted situation where, in the case of *Ma3*, melting is dominated by the
666 consumption of biotite and quartz and garnet growth in the solid as a peritectic phase, while in
667 the case of *Ma5*, cordierite and Kfs contribute significantly to melting in addition to biotite, in the
668 absence of garnet. In the first case, the bulk partition coefficients for REE vary from 0.30 (Sm) to
669 12.17 (Lu) while in the second case, they vary from 0.89 (Sm) to 2.78 (La) (Table 6), *i.e.* in the
670 first case, the LREE and MREE will behave as slightly incompatible elements whereas the HREE
671 will behave as compatible elements, whereas in the second case, all REE but Sm and Yb will
672 behave as compatible elements during partial melting. In both cases, the bulk partition
673 coefficients for transition elements are much higher than 1 and are generally higher in the case of
674 *Ma3*. As a result, there will be very little variation in the trace element content of the residual
675 solid Cs compared to the initial solid C_0 during partial melting at the considered temperature,
676 where the melt fraction does not exceed 20%. The Cs/C_0 is in the range 0.7 to 1.23 and 0.96 to

1.1 respectively for REE for model 1 and model 2, and is in the range 1.14 to 1.23 and 1.05 to 1.15 for transition elements (Table 6). This is much lower than the observed variations among xenoliths (Fig. 9, Table 5), where the REE content varies by a factor of 4.5 to 7.5 depending on the REE and the transition element content by a factor of 2.1 to 2.9. Thus, the chemical diversity among xenolith cannot be attributed to different degrees of partial melting and melt extraction due to their incorporation in the magma. The diversity in major and trace element composition must be attributed to the diversity of their metapelitic protoliths. Thus, the protolith from which xenoliths have been derived must have undergone first partial melt extraction to explain their variable depletion in SiO_2 and enrichment in Al_2O_3 compared to standard metapelites. This must have taken place before entrapment in the magmas, *i.e.* during either earlier regional metamorphism or contact metamorphism related magma emplacement, as will be discussed below. This conclusion is in line with those proposed by other authors (*e.g.* Aguilar *et al.*, 2016) that multiple melt extraction is necessary to shift the composition of the solid residue toward marked refractory composition.

10. Xenoliths as witnesses of metamorphic conditions of late Hercynian metamorphism in Moroccan Meseta

Three types of xenoliths can be distinguished based on their pressure-temperature record (Fig. 17). The first type, represented by samples *Ma3* and *Ma10*, record pressures higher than 5 kbar (as demonstrated by the presence of garnet) for temperatures exceeding 800°C (as demonstrated by the presence of spinel associated to partial melting). A decompression path at high temperature is recorded in both samples by the transformation of garnet into cordierite. The second type, represented by sample *Ma5*, records intermediate pressure of ca 3 kbar for a temperature of 750 to 800 °C. Few garnet relics surrounded by a corona of cordierite testify for limited heating / decompression path. At last, samples *Ma6* and *Kar2b* exemplify a third type of xenoliths, that record low pressure (<2.5 kbar), as demonstrated by the abundance of andalusite relics and the absence of garnet. The transformation of an initial andalusite bearing assemblage into a sillimanite-corundum-spinel-cordierite assemblage associated to partial melting records a major heating from below 700°C to *ca.* 900°C at constant pressure.

As a whole, the xenoliths have thus sampled a crustal segment from *ca. 5* to 25 km (Fig. 17), considering a lithostatic pressure and a density of 2700 kg.m^{-3}. The overall pressure range recorded by the xenoliths matches the pressure range recorded by metamorphic rocks outcropping in the Rehamna (6 to 9 kbar; Aghzer et Arenas, 1998; Wernert *et al*., 2016), in the Jebilet (1.5 to 5 kbar; Delchini *et al*., 2016) and in the Eastern Meseta (6 kbar, Elabouyi *et al*., 2019) and by the crustal xenoliths in late Hercynian magmas from the Jebilet (3 kbar, Bouloton *et al.,* 1991), in the Middle Atlas (9-11 kbar; Moukadiri and Bouloton, 1998), and in the Zaër pluton (2-5 kbar, Haïmeur *et al.*, 2003). The absence of xenoliths recording a pressure higher than 11 kbar suggests either that the lower crustal levels have not been sampled by the magmas coming from the underlying mantle or that the Hercynian orogenic crust was only moderately thickened (less than 40 km) in the area.

Based on geochemical and isotopic data, it has been argued that the analogue Permian granodioritic magmas have a mixed mantle-crustal origin with limited crustal component ($^{87}Sr/^{86}Sr$ up to 0.705; Mrini *et al.*, 1992, for the Central Massif and the Rehamna; Gasquet *et al*., 1992 for the Tichka Massif; Youbi *et al*., 2001 and Dostal *et al*., 2005 for the dykes of the Jebilet). This is confirmed by the trace element data on the microgranodiorite and microgranite dykes from Kariane that show a marked negative Nb–Ta anomaly that can best be explained by crustal contamination in a late orogenic context.

The *PT* conditions recorded by the xenoliths corresponding to the maximum temperature are consistently in the range 800 to 900 °C, regardless of the pressure. Moreover, in xenoliths *Ma3* and *Ma10,* which record the highest pressure (*ca.* 6 kbar), the temperature associated to the earliest metamorphic stage (>850 °C) is higher than the metamorphic temperature at the same pressure reported from regional metamorphism associated to the orogenic stages in the D1- D2 deformation events in the Rehamna (Aghzer et Arenas, 1998; Wernert *et al*., 2016), in the Jebilet (Delchini *et al*., 2016) and in the Eastern Moulouya (Elabouyi *et al*. 2019) (Fig. 17). This suggests that the maximal temperature records thermal metamorphism associated to the incorporation into the magma, as already suggested by Bouloton *et al*. (1991). The peak-temperature range (800-900 °C) recorded by the xenoliths lies in between the solidus (700-800 °C) and liquidus (900-1000 °C) temperatures calculated for the host magmas (Table 5) over

739 the pressure range of 1-6 kbar with MELTS-Excel sheet (Gualda and Ghiorso, 2015). Given the
740 small size of the xenoliths (<10 cm), thermal equilibrium between the host magma and the
741 xenolith should be achieved in less than one day. On the other hand, the persistence of andalusite
742 in a metastable form suggests a short metamorphic history. This is consistent with the
743 characteristic cooling time t of *ca.* 10 days that can be estimated for a dyke of half-thickness d of
744 1 m considering a thermal diffusivity K of *ca.* 1×10^{-6} m^2 s^{-1} and a conductive model where
745 $t = d^2/(4K)$ (Turcotte and Schubert, 2003). The pressures and temperatures recorded by the
746 xenoliths in Kariane are in good agreement with those reported in xenoliths in other places in
747 Morocco (Fig. 17). The xenoliths in Oulad Ouaslam (Jebilet) described by Bouloton *et al* (1991)
748 record *PT* conditions of *ca.* 750 °C, 3 kbar, similar to xenolith *Ma5*. The xenoliths from the Zaër
749 pluton (Central Massif) studied by Haïmeur *et al*. (2003) record *PT* conditions of 600-650 °C, 2
750 to 2.5 kbar for andalusite-bearing xenoliths, similar to xenoliths *Ma6* and *Kar2b,* while
751 corundum-spinel-bearing xenoliths record *PT* conditions of 690-770°C, 4 to 5 kbar, similar to
752 samples *Ma3* and *Ma10*. The *PT* conditions retrieved from migmatitic terrains associated to both
753 M-I type and S-type magmatism in the so-called Colline à Essaim d'Enclaves of the Eastern
754 Meseta by Elabouyi *et al*. (2019) record an isobaric heating history with maximal *PT* condition in
755 full agreement with those recorded by samples *Ma3* and *Ma10*. At last, granulitic xenoliths from
756 Plio-Quaternary basalts from the Middle Atlas record the highest pressures (9-11 kbar) for
757 temperatures of *ca.* 900 °C similar to those of samples *Kar2b* and *Ma6.* In the case of the
758 xenoliths from the Kariane locality, the age of the magmatic event responsible for the entrapment
759 of the xenoliths in the dykes and the associated metamorphism is not well constrained. It can be
760 attributed to the Permian both on stratigraphic grounds and on previous radiometric dating
761 (Cheilletz, 1984; Rossi *et al*., 2016). The ages obtained in the present study on monazites from
762 the xenolith (EPMA age of 293 ± 25 Ma) are consistent with those earlier age estimates.
763
764 The retrieval of the *PT* conditions that prevailed before the incorporation of the xenolith into the
765 magma is difficult to assess. Regional metamorphism or syn-tectonic contact metamorphism is
766 attested in the xenoliths from the Kariane locality by the oriented sillimanite-biotite-garnet
767 association in sample *Ma3*, but the pressure-temperature record is obliterated by the temperature
768 increase due to the entrapment in the magma. The early andalusite-bearing paragenesis in
769 samples *Ma6* and *Kar2b* records pressures and temperature conditions of *ca.* 600 °C for a

pressure lower than 2.5 kbar, which is consistent both with the *PT* estimates of some of the xenoliths from the Zaër Pluton (Haïmeur *et al*., 2003) and with the temperature and pressure associated to contact metamorphism in amphibolite facies in metapelites from the Jebilet Massif by Delchini *et al*. (2016). However, in sample *Ma10*, the presence of andalusite chiastolite attesting for an early contact metamorphism implies *a priori* a pressure lower than 4 kbar, which is not consistent with the peak *PT* conditions (>4.5 kbar). This discrepancy may be explained either by a burial of the sample after contact metamorphism and before entrapment in the magma (orange line in Fig. 17), or if we admit a high-pressure high-temperature position for the silicate triple point (4.5 ± 0.5 kbar, 550 ± 35 °C) (Pattison, 1992; Cesare *et al.*, 2003) rather than the position of the triple point from Holland and Powell (1998) data base used in the thermodynamic models (Fig.17). In the latter case, slightly higher *P* and *T* conditions for the early andalusite-bearing stages are retrieved both for samples *Ma6* and *Kar2b* (*ca.* 700 °C for a pressure lower than 2.5 kbar) and the prograde evolution of sample *Ma10* can be explained by isobaric heating from 550°C toward 800 °C at *ca.* 4.5 kbar (dashed orange line in Fig. 17). There is no available dating of those initial stages of metamorphism, which can represent either the early stage of heating and incorporation in the Permian dykes, or a former stage of contact metamorphism of the metasedimentary protoliths due to the intrusion of Carboniferous to Permian granitoids, such as described in the Jebilet, in the Rehamna, or in the neighbouring granitoid of Ment (*e.g.* Dahmani, 1995; Chopin *et al*., 2014; Delphini *et al.,* 2016). Both regional metamorphism of the protolith and a pre-entrapment contact metamorphism and could have promoted early partial melting and melt extraction from the metasedimentary protolith and explain their refractory nature.

11. Conclusion

A suite of metapelitic xenoliths enclosed in a micro-quartz diorite dyke from the Moroccan Central Massif records granulite facies metamorphism, with maximal temperatures of 800 °C to 900 °C. Peak pressure conditions varying from *ca.* 1.5 to 6 kbar depending on the xenolith. Stratigraphic constrains assign a Permian age for the micro-quartz diorite dyke, whereas U-Th/Pb EPMA dating on monazite in the xenoliths gives a date of 293 ± 25 Ma which, although poorly defined, confirms a late Variscan age for this metamorphism. The xenoliths therefore sample the

first 25 km of the Variscan crust. However, the recorded maximal temperatures are systematically higher than the temperatures of the regional metamorphism associated to the Variscan tectono-metamorphic history. It is therefore concluded that the high temperature recorded in the xenoliths results from heating by the hot granodioritic host magmas.

The chemistry of the metapelitic xenoliths is generally silica-poor, aluminum-rich, which results in peculiar metamorphic quartz-absent assemblages comprising aluminosilicate (andalusite ± sillimanite), corundum, spinel, cordierite and sometimes garnet. Although partial melt may have escaped the xenolith during entrapment in the magma, it is shown that melt loss cannot explain the refractory conditions observed in the xenoliths. The protoliths must therefore have been preconditioned by regional metamorphism or previous contact metamorphism at high temperature condition by a first depletion due to partial melting and melt loss. The remnants of this initial metamorphic stage can be found in the presence of andalusite, biotite and garnet crystals in some xenoliths.

Acknowledgements

This project has been founded by CNRS –INSU - SYSTER program, by the University of Toulouse through an international partneship with University Sidi Mohamed Ben Abdellah in Fez, Morocco. We are grateful to the head and members of the departement of geology of the University Sidi Mohamedb Ben Abdellah of Fès for their support and welcome during meetings and field work. Many thanks to Antonio Álvarez-Valero, Ingrid van Namen and Joost van Hoeflaken who participated to this early field work and sampling in Morocco. This publication has been improved by the careful and constructive reviews of Bernardo Cesare and an anonymous reviewer.

827 **References**

828 Accotto, C., Martínez Poyatos, D., Azor, A., Jabaloy-Sánchez, A., Talavera, C., Evans, N.J.,
829 Azdimousa, A., 2020. Tectonic Evolution of the Eastern Moroccan Meseta: From Late
830 Devonian Forearc Sedimentation to Early Carboniferous Collision of an Avalonian
831 Promontory. Tectonics 39, e2019TC005976.
832 Acosta-Vigil, A., Buick, I.S., Hermann, J., Cesare, B., Rubatto, D., London, D., Morgan, G.B.,
833 2010. Mechanisms of Crustal Anatexis: a Geochemical Study of Partially Melted
834 Metapelitic Enclaves and Host Dacite, SE Spain. Journal of Petrology 51, 785-821.
835 Aghzer, A.M., Arenas, R., 1995. Détachements et tectonique extensive dans le massif hercynien
836 des Rehamna (Maroc). Journal of African Earth Sciences 21, 383-393.
837 Aghzer, A.M., Arenas, R., 1998. Evolution métamorphique des métapélites du Massif hercynien
838 des Rehamna (Maroc): implications tectonothermales. Journal of African Earth Sciences
839 27, 87-106.
840 Aguilar, C., Liesa, M., Reche, Powell, R., 2016. Fluid-fluxed melting and melt loss in a
841 syntectonic contact metamorphic aureole from the Variscan eastern Pyrenees. Journal of
842 Metamorphic Geology 34, 379-400.
843 Álvarez-Valero, A.M. and Kriegsman, L.M., 2007. Crustal thinning and mafic underplating
844 beneath the Neogene Volcanic Province (Betic Cordillera, SE Spain): evidence from
845 crustal xenoliths. Terra Nova, 19: 266-271.
846 Álvarez-Valero, A.M., Cesare, B., Kriegsman, L.M., 2007. Formation of spinel-cordierite-
847 feldspar-glass coronas after garnet in metapelitic xenoliths: reaction modelling and
848 geodynamic implications. Journal of Metamorphic Geology 25, 305-320.
849 Álvarez-Valero, A.M., Waters, D.J., 2010. Partially Melted Crustal Xenoliths as a window into
850 Sub-Volcanic Processes: Evidence from the Neogene Magmatic Province of the Betic
851 Cordillera, SE Spain. Journal of Petrology 51, 973-991.
852 Álvarez-Valero, A.M., Pla, F., Kriegsman, L.M., Geyer, A., Herrero, H., 2015. Observing silicic
853 magma transport in dykes at depths of 8–19km: Evidences from crustal xenoliths and
854 numerical modelling. Journal of Volcanology and Geothermal Research 296, 69-79.
855 Bea, F., Pereira, M.D., Stroh, A., 1994. Mineral/leucosome trace-element partitioning in a
856 peraluminous migmatite (a laser ablation-ICP-MS study). Chemical Geology 117, 291-
857 312.

Ben Abbou, M., Soula, J.-C., Brusset, S., Roddaz, M., Ntarmouchant, A., Driouch, A., Christophoul, F., Bouadbelli, M., Majesté-Menjoulas, C., Béziat, D., Debat, P., Déramond, J., 2001. Contrôle tectonique de la sédimentation dans le système de bassins d'avant-pays de la Meseta marocaine. Comptes Rendus de l'Académie des Sciences - Series IIA - Earth and Planetary Science 332, 703-709.

Berman, R.G., Aranovitch, L.Y., 1996. Optimized standard state and solution properties of minerals. I. Model calibration for olivine, orthopyroxene, cordierite, garnet, and ilmenite in the system FeO-MgO-CaO-Al_2O_3-SiO_2-TiO_2-H_2O-CO_2. Contributions to Mineralogy and Petrology 126, 1-24.

Boushaba, A., Cailleux, Y., 1992. Les relations métamorphisme-déformation au voisinage des granitoïdes hercynien du Maroc central. Bull. Inst. Sci., Rabat 16, 15-22.

Bouloton J., El Amrani I. El Mouraouah A. et Montel J. M., 1991. Les xénolithes hyperalumineux des granites, d'après l'exemple du pluton superficiel des Oulad Ouslam (Jbilet, Maroc). C. R. Acad. Sci. Paris, 231, pp. 273-279.

Bouloton, J., Gasquet, D., 1995. Melting and undercooled crystallisation of felsic xenoliths from minor intrusions (Jebilet massif, Morocco). Lithos 35, 201-219.

Buick, I.S., Stevens, G., Gibson, R.L., 2004. The role of water retention in the anatexis of metapelites in the Bushveld Complex Aureole, South Africa: an experimental study. Journal of Petrology 45, 1777-1797.

Carignan, J., Hild, P., Mevelle, G., Morel, J., Yeghicheyan, D., 2001. Routine Analyses of Trace Elements in Geological Samples using Flow Injection and Low Pressure On-Line Liquid Chromatography Coupled to ICP-MS: A Study of Geochemical Reference Materials BR, DR-N, UB-N, AN-G and GH. Geostandards Newsletter 25, 187-198.

Cesare, B., 2000. Incongruent melting of biotite to spinel in a quartz-free restite at El Joyazo (SE Spain): Textures and reaction characterization. Contributions to Mineralogy and Petrology 139, 273-284.

Cesare, B., Marchesi, C., Hermann, J., Gómez-Pugnaire, M.T., 2003. Primary melt inclusions in andalusite from anatectic graphitic metapelites: Implications for the position of the Al2SiO5 triple point. Geology 31, 573-576.

887 Cheilletz, A., 1984 – Contribution à la gitologie du district polymétallique (W, Mo, Cu, Zn, Ag)
888 du Djebel Aouam (Maroc Central, application à la prospection des gisements de
889 tungstène). Thèse de doctorat ès-Sciences, I.P.T.L, Nancy. 250 p.
890 Chopin, F., Corsini, M., Schulmann, K., El Houicha, M., Ghienne, J.-F., Edel, J.-B., 2014.
891 Tectonic evolution of the Rehamna metamorphic dome (Morocco) in the context of the
892 Alleghanian-Variscan orogeny. Tectonics 33, 1154-1177.
893 Coggon, R., Holland, T.J.B., 2002. Mixing properties of phengitic micas and revised garnet-
894 phengite thermobarometers. Journal of Metamorphic Geology 20, 683-696.
895 Connolly, J.A.D., 2005. Computation of phase equilibria by linear programming: a tool for
896 geodynamic modeling and its application to subduction zone decarbonation. Earth and
897 Planetary Science Letters 236, 524–541.
898 Connolly, J.A.D., 2009. The geodynamic equation of state: What and how. Geochemistry,
899 Geophysics, Geosystems 10, Q10014.
900 Corsini, M., Rolland, Y., 2009. Late evolution of the southern European Variscan belt:
901 Exhumation of the lower crust in a context of oblique convergence. Comptes Rendus
902 Geoscience 341, 214-223.
903 Cox, K. G., Bell, J. D. & Pankhurst, R. J. (1979). The Interpretation of Igneous Rocks. London:
904 George Allen & Unwin. pp 450
905 Dahmani, A. (1995). Développement des auréoles de contact d'Oulmès et de Ment (Maroc
906 Central): étendue, zones métamorphiques et histoires de réchauffement et de
907 refroidissement. Chicoutimi, PhD thesis. Université du Québec.
908 Depine, G.V., Andronicos, C.L., Phipps-Morgan, J., 2008. Near-isothermal conditions in the
909 middle and lower crust induced by melt migration. Nature 452, 80-83.
910 Delchini, S., Lahfid, A., Lacroix, B., Baudin, T., Hoepffner, C., Guerrot, C., Lach, P., Saddiqi,
911 O., and Ramboz, C., 2018, The Geological Evolution of the Variscan Jebilet Massif,
912 Morocco, Inferred From New Structural and Geochronological Analyses. Tectonics 37,
913 4470-4493.
914 Delchini, S., Lahfid, A., Plunder, A., and Michard, A., 2016, Applicability of the RSCM
915 geothermometry approach in a complex tectono-metamorphic context: The Jebilet massif
916 case study (Variscan Belt, Morocco). Lithos 256–257, 1–12.

Díaz-Alvarado, J., Castro, A., Fernández, C., Moreno-Ventas, I., 2011. Assessing bulk assimilation in cordierite-bearing granitoids from the Central System Batholith, Spain; experimental, geochemical and geochronological constraints. Journal of Petrology 52, 223-256.

Dostal, J., Keppie, J.D., Hamilton, M.A., Aarab, E.M., Lefort, J.P., Murphy, J.B., 2005. Crustal xenoliths in Triassic lamprophyre dykes in western Morocco: tectonic implications for the Rheic Ocean suture. Geological Magazine 142, 159–172.

Duchene, S., Fornelli, A., Micheletti, A.-M., Piccarreta, G., 2013. Sm-Nd chronology of porphyroblastic garnets from granulite facies metabasic rocks in Calabria (Southern Italy): inferences for preserved isotopic memory and resetting. Mineralogy and Petrology 107, 539-551.

Elabouyi, M., Dahire, M., Driouch, Y., Duchêne, S., Kriegsman, L.M., Ntarmouchant, A., Kahou, Z.S., Severac, J.L., Belkasmi, M., Debat, P., 2019. Crustal anatexis in the Aouli-Mibladen granitic complex: A window into the middle crust below the Moroccan Eastern Variscan Meseta. Journal of African Earth Sciences 154, 136-163.

Elkins, L.T., Grove, T.L., 1990. Ternary feldspar experiments and thermodynamic models. American Mineralogist 75, 544-559.

England, P.C., Thompson, A.B., 1984. Pressure-Temperature-time path of regional metamorphism: I Heat transfer during the evolution of regions of thickened metamorphic rocks. Journal of Petrology 25, 894-928.

Essaifi, A., Potrel, A., Capedevila, R., Lagarde, J.-L., 2003. U–Pb dating: emplacement age of the bimodal magmatism of central Jebilet (Variscan Belt, Morocco). Geodynamic implications. Comptes Rendus Géoscience 335, 193–203.

Fornelli, A., Langone, A., Micheletti, A.-M., Piccarreta, G., 2011. Time and duration of Variscan high-temperature metamorphic processes in the south European Variscides: constraints from U-Pb chronology and trace element chemistry of zircon. Mineralogy and Petrology 103, 101–122.

Gasquet, D., Leterrier, J., Mrini, Z., Vidal, P., 1992. Petrogenesis of the Hercynian Tichka plutonic complex (Western High Atlas, Morocco): Trace element and Rb-Sr and Sm-Nd isotopic constraints. Earth and Planetary Science Letters 108, 29-44.

947 Gasquet, D., Bertrand, J.-M., Paquette, J.-L., Lehmann, J.r.m., Ratzov, G., De Ascenção Guedes,
948 R., Tiepolo, M., Boullier, A.-M., Scaillet, S., Nomade, S., 2010. Miocene to Messinian
949 deformation and hydrothermal activity in a pre-Alpine basement massif of the French
950 western Alps: new U-Th-Pb and argon ages from the Lauzière massif. Bulletin de la
951 Société Géologique de France 181, 227-241.
952 Gonçalves, G.O., Lana, C., Scholz, R., Buick, I.S., Gerdes, A., Kamo, S.L., Corfu, F., Marinho,
953 M.M., Chaves, A.O., Valeriano, C., Nalini, H.A., Jr., 2016. An assessment of monazite
954 from the Itambe pegmatite district for use as U-Pb isotope reference material for
955 microanalysis and implications for the origin of the "Moacyr" monazite. Chemical
956 Geology 424, 30-50.
957 Graessner, T., Schenk, V., 2001. An exposed Hercynian deep crustal section in the Sila Massif of
958 Northern Calabria: mineral chemistry, petrology, and P-T path of granulite-facies
959 metapelitic migmatites and metabasites. Journal of Petrology 42, 931-961.
960 Gualda, G.A.R., Ghiorso, M.S., 2015. MELTS_Excel: A Microsoft Excel-based MELTS
961 interface for research and teaching of magma properties and evolution. Geochemistry,
962 Geophysics, Geosystems 16, 315-324
963 Guitard, G., Vielzeuf, D., Martinez, F., 1995. Synthèse Géologique et Géophysique des Pyrénées
964 - Le Métamorphisme Hercynien, pp. 501-584.
965 Haïmeur, J., Chabane, A., El Amrani El Hassani, I.-E., 2003. Analyse pétro-minéralogique des
966 interactions granite-enclaves dans le pluton hercynien de Zaër (Maroc central) :
967 implications pétrogénétiques. Bulletin de l'Institut Scientifique, Rabat, section Sciences
968 de la Terre n°25, 1-29.
969 Hoepffner, C., Soulaimani, A., Piqué, A., 2005. The Moroccan Hercynides. Journal of African
970 Earth Sciences 43, 144-165.
971 Holland, T., Powell, R., 1998. An internally consistent thermodynamic data set for phases of
972 petrological interest. Journal of Metamorphic Geology 16, 309-343.
973 Janoušek, V., Farrow, C.M., Erban, V., 2006. Interpretation of whole-rock geochemical data in
974 igneous geochemistry: introducing Geochemical Data Toolkit (GCDkit). Journal of
975 Petrology 47, 1255-1259.

976 Johnson, T., Brown, M., Gibson, R. & Wing, B., 2004. Spinel cordierite symplectites replacing
977 andalusite: evidence for melt assisted diapirism in the Bushveld Complex, South Africa.
978 Journal of Metamorphic Geology, 22, 529–545.
979 Johnson, T.E., Brown, M., White, R.W., 2010. Petrogenetic modelling of strongly residual
980 metapelitic xenoliths within the southern Platreef, Bushveld Complex, South Africa.
981 Journal of Metamorphic Geology 28, 269-291.
982 Johnson, T.E., White, R.W., Brown, M., 2011. A year in the life of an aluminous metapelite
983 xenolith—The role of heating rates, reaction overstep, H_2O retention and melt loss. Lithos
984 124, 132-143.
985 Juez-Larré, J., Ter Voorde, M., 2009. Thermal impact of the break-up of Pangea on the Iberian
986 Peninsula, assessed by thermochronological dating and numerical modelling.
987 Tectonophysics 474, 200–213.
988 Kunz, B.E., Manzotti, P., von Niederhäusern, B., Engi, M., Darling, J.R., Giuntoli, F., Lanari, P.,
989 2018. Permian high-temperature metamorphism in the Western Alps (NW Italy).
990 International Journal of Earth Sciences 107, 203-229.
991 Lahfid, A., Baidder, L., Ouanaimi, H., Soulaimani, A., Hoepffner, C., Farah, A., Saddiqi, O.,
992 Michard, A., 2019. From extension to compression: high geothermal gradient during the
993 earliest Variscan phase of the Moroccan Meseta; a first structural and RSCM
994 thermometric study. European Journal of Mineralogy 31, 695-713.
995 Martínez Catalán, J. R., K. Schulmann, et al. (2021). "The Mid-Variscan Allochthon: Keys from
996 correlation, partial retrodeformation and plate-tectonic reconstruction to unlock the
997 geometry of a non-cylindrical belt." Earth-Science Reviews 220: 103700.
998 McDonough, W.F., Sun, S., 1995. The composition of the Earth. Chemical Geology 120, 223-
999 253.
1000 Michard, A., Hoepffner, C., Soulaimani, A., Baidder, L., 2008. The variscan belt, In: Michard, A.
1001 (Ed.), Continental Evolution: The Geology of Morocco. Springer-Verlag, Berlin
1002 Heidelberg, pp. 65-132.
1003 Michard, A., Soulaimani, A., Hoepffner, C., Ouanaimi, H., Baidder, L., Rjimati, E.C., Saddiqi,
1004 O., 2010. The South-Western Branch of the Variscan Belt: Evidence from Morocco.
1005 Tectonophysics 492, 1–24.

1006 Montel, J.-M., Foret, S., Veschambre, M., Nicollet, C., Provost, A., 1996. Electron microprobe
1007 dating of monazite. Chemical Geology 131, 37–53.
1008 Moukadiri, A., Bouloton, J., 1998. Pétrologie des granulites exhumées par le volcanisme récent
1009 du Moyen Atlas : aperçu sur la croûte inférieure néogène du Maroc central. Comptes
1010 Rendus de l'Académie des Sciences - Series IIA - Earth and Planetary Science 327, 731-
1011 734.
1012 Mrini, Z., Rafi, A., Duthou, J.L., Vidal, P., 1992. Chronologie Rb-Sr des granitoides hercyniens
1013 du Maroc; consequences. Bulletin de la Société Géologique de France 163, 281-291.
1014 Nakamura, N., 1974. Determination of REE, Ba, Fe, Mg, Na and K in carbonaceous and ordinary
1015 chondrites. Geochimica et Cosmochimica Acta 38, 757-775.
1016 Newton, R.C., Charlu, T.V., Kleppa, O.J., 1980. Thermochemistry of the high structural state
1017 plagioclases. Geochimica et Cosmochimica Acta 44 933-941.
1018 Ntarmouchant, A., 2003. Le magmatisme associé aux bassins carbonifères d'avant-pays :
1019 Exemple du magmatisme bassin méridional d'Azrou-Khénifra (Est du Maroc Hercynien
1020 Central). Nature métasédimentaire du soubassement, contexte de mise en place et
1021 implication géodynamique. Thèse ès sciences, Université Sidi Mohammed Ben Abdellah,
1022 Fès, 312p.
1023 Patiño Douce, A.E., Johnson, A.D., 1991. Phase equilibria and melt productivity in the pelitic
1024 system: implications for the origin of peraluminous granitoids and aluminous granulites.
1025 Contributions to Mineralogy and Petrology 107, 2020-2218.
1026 Pattison, D.R.M., 1992. Stability of Andalusite and Sillimanite and the Al2SiO5 Triple Point:
1027 Constraints from the Ballachulish Aureole, Scotland. The Journal of Geology 100, 423-
1028 446.
1029 Petri, B., Mohn, G., Skrzypek, E., Mateeva, T., Galster, F., Manatschal, G., 2017. U–Pb
1030 geochronology of the Sondalo gabbroic complex (Central Alps) and its position within the
1031 Permian post-Variscan extension. International Journal of Earth Sciences 106, 2873-2893.
1032 Piqué, A., Michard, A., 1989. Moroccan Hercynides, a synopsis. The Palaeozoic sedimentary and
1033 tectonic evolution at the northern margin of West Africa. American Journal of Science
1034 289, 286–330.
1035 Powell, R. & Downes, J., 1990. Garnet porphyroblast-bearing leucosomes in metapelites:
1036 mechanisms, phase diagrams, and an example from Broken Hill, Australia. In: High-

Temperature Metamorphism and Crustal Anatexis (eds Ashworth, J.R. & Brown, M.), pp. 105–123. Unwin, London

Roddaz, M., Brusset, S., Soula, J.-C., Béziat, D., Ben Abbou, M., Debat, P., Driouch, Y., Christophoul, F., Ntarmouchant, A., Déramond, J., 2002. Foreland basin magmatism in the Western Moroccan Meseta and geodynamic inferences. Tectonics 21, 7-1-7-23.

Rossi, P., Cocherie, A., Fanning, C.M., 2015. Evidence in Variscan Corsica of a brief and voluminous Late Carboniferous to Early Permian volcanic-plutonic event contemporaneous with a high-temperature/low-pressure metamorphic peak in the lower crust. Bulletin de la Société Géologique de France 186, 171-192.

Rossi, M., Tarrieu, L., Cheilletz, A., Gasquet, D., Deloule, E., Paquette, J.-L., Bounajma, H., Mantoy, T., Ouazzani, L., Ouchtouban, L., 2016. The Polymetallic (W–Au and Pb–Zn–Ag) Tighza District (Central Morocco): Ages of Magmatic and Hydrothermal Events, in Bouabdellah, M., Slack, J.F. (Eds.) Mineral Deposits of North Africa. Mineral Resource Reviews, pp. 107-131.

Seydoux-Guillaume, A.M., Wirth, R., Nasdala, L., Gottschalk, M., Montel, J.M., Heinrich, W., 2002. An XRD, TEM and Raman study of experimentally annealed natural monazite. Physics and Chemistry of Minerals 29, 240-253.

Seydoux-Guillaume A-M, Montel J-M, Bingen B, Bosse V, de Parseval P, Paquette J-L, Janots E, Wirth R., 2012. Low-temperature alteration of monazite: Fluid mediated coupled dissolution–precipitation, irradiation damage, and disturbance of the U–Pb and Th–Pb chronometers. Chemical Geology 330- 331:140–158.

Simancas, J.F., Tahiri, A., Azor, A., González-Lodeiro, F., Martínez-Poyatos, D., El Hadi, H., 2005. The tectonic frame of the Variscan–Alleghanian orogen in Southern Europe and Northern Africa. Tectonophysics 398, 181-198.

Simancas, J.F., Azor, A., Martínez-Poyatos, D., Tahiri, A., El Hadi, H., González-Lodeiro, F., Pérez-Estaún, A., Carbonell, R., 2009. Tectonic relationships of Southwest Iberia with the allochthons of Northwest Iberia and the Moroccan Variscides. Comptes Rendus Geoscience 341, 103-113

Siron, G., Goncalves, P., Marquer, D., Pierre, T., Paquette, J.-L., Vanardois, J., 2020. Contribution of magmatism, partial melting buffering and localized crustal thinning on the

late Variscan thermal structure of the Agly massif (French Pyrenees). Journal of Metamorphic Geology 1-31.

Stampfli, G.M., Borel, G.D., 2002. A plate tectonic model for the Paleozoic and Mesozoic constrained by dynamic plate boundaries and restored synthetic oceanic isochrons. Earth and Planetary Science Letters 196, 17-33.

Tajčmanová, L., Connolly, J.A.D., Cesare, B., 2009. A thermodynamic model for titanium and ferric iron solution in biotite. Journal of Metamorphic Geology 27, 153-165.

Turcotte, D.L., Schubert, L., 2003. Geodynamics. Cambridge University Press 456 pp

van Hoeflaken, J., 2011. Hercynian UHT metamorphism of crustal xenoliths from Bou Ibalghatene and Tafraoute, Middle Atlas, Morocco. Unpublished MSc Thesis, Utrecht University.

Vielzeuf, D., Holloway, J.R., 1988. Experimental determination of the fluid-absent melting relations in the pelitic system. Contributions to Mineralogy and Petrology 98, 257-276.

Villa-Vialaneix N., Montel J.-M. and Seydoux-Guillaume A.-M. (2013) NiLeDAM: Monazite Datation for the NiLeDAM team. R package version 0.1.

Waldbaum, D.R., Thompson, J.B., 1968. Mixing properties of sanidine crystalline solutions : II Calculations based on volume data. American Mineralogist 53, 2000-2017.

Wernert, P., Schulmann, K., Chopin, F., Štípská, P., Bosch, D., El Houicha, M., 2016. Tectonometamorphic evolution of an intracontinental orogeny inferred from P–T–t–d paths of the metapelites from the Rehamna massif (Morocco). Journal of Metamorphic Geology 34, 917-940.

White, R.W.P., R., Holland, J.B., Worley, B., 2000. The effect of TiO_2 and Fe_2O_3 on metapelitic assemblages at greenschist and amphibolite facies conditions: mineral equiibria calculations in the system K_2O-FeO-MgO-Al_2O_3-SiO_2-H_2O-TiO_2-Fe_2O_3. Journal of Metamorphic Geology 18, 497-511.

White, R.W., Powell, R., Holland, J.B., 2001. Calculation of partial melting equilibria in the system Na_2O-CaO-K_2O-FeO-MgO-Al_2O_3-SiO_2-H_2O (NCKFMASH). Journal of Metamorphic Geology 19, 139-153.Whitney, D.L., Evans, B.W., 2010. Abbreviations for names of rock-forming minerals. American Mineralogist 95, 185-187.

Youbi, N., Bellon, H., Marzin, A., Piqué, A., Cotten, J., Cabanis, B., 2001. Du cycle orogénique hercynien au pré-rifting de l'Atlantique central au Maroc occidental : les microdiorites des

Jbilet sont-elles des marqueurs magmatiques de ce passage ? Comptes Rendus de l'Académie des Sciences - Series IIA - Earth and Planetary Science 333, 295-302.

Figure Captions

Fig. 1 Geological maps (a) Tectonic map of Morocco and location of the study area (b) Geological map of the study area (d'après Ntarmouchant, 2003)

Fig. 2 Field photographs of the sampling area (Kariane locality) (a) Field view of the microgranodioritic dyke (b) Contact between the dyke and the Ordovician metasediments (c, d) Two examples of crustal xenoliths in the microgranodioritic host rock

Fig. 3 Photomicrographs showing the assemblages and microstructures within the xenoliths. (a) *Ma3* Foliation underlined by sillimanite, skeletal biotite and elongated corroded garnet grains with sillimanite needles underlining and internal schistosity. Note the large cordierite flake enfolding all other mineral phases. (b) *Ma3* Note the presence of spinel overprinting the foliation. (c) *Ma10* Large chiastolitic andalusite prisms surrounded by a spinel + plagioclase corona. (d) *Ma10* Broken enbay crystal partly transformed into sillimanite and surrounded by a spinel-rich corona; cordierite corona surrounding garnet; plagioclase corona surrounding spinel. (e) *Ma6* Crystal of andalusite partially replaced by sillimanite and plagioclase; plagioclase contains spinel and separates andalusite from cordierite (f) *Ma6* Andalusite pseudomorph including corundum and transformed into plagioclase. (g) *Ma6* Plagioclase-spinel matrix displaying magmatic texture. (h) *Kar2b* Corundum and spinel within plagioclase replacing andalusite. (i) *Ma5* Plagioclase pseudomorphose of a crystal of andalusite (square section is recognizable). (j) *Ma5* Plagioclase euhedral twinned crystals with Spl inclusions. (k) *Ma5* Corundum rimmed by cordierite and spinel. (l) *Ma5* Corroded garnet grain rimmed by brown cordierite flakes. Mineral abbreviations from Whitney and Evans (2010).

Fig. 4 BSE images and EDS maps of the xenoliths. (a,g) *Ma3.* Note oriented inclusions of sillimanite and ilmenite in garnet and the K enrichment at alkali feldspar boundaries (b) *Ma10* Feldspar – cordierite rims at garnet crystal. Note the complex alkali-feldspar / plagioclase concentric pattern (c) *Ma10* Plagioclase – alkali feldspar association filling microcracks in andalusite crystal (d) *Ma6* Andalusite crystals resorbed into a plagioclase – spinel association (d) *Kar2b* Andalusite crystals resorbed into a plagioclase – spinel association (f) *Ma5* Note resorbed corundum in a plagioclase matrix and the presence of cordierite. Quantitative EDS maps (g, j, k, l) have been used to quantify local composition for thermodynamical modelling . Mineral abbreviations from Whitney and Evans (2010).

Fig. 5 Mineral chemistry a) Ternary diagram for feldspar with solvus isotherms at 5 kbar from Elkins and Grove (1990) (b) $Ti+Al^{VI} = f(Fe+Mg)$ diagram for biotite.

Fig. 6 Photomicrographs of the host rock and contacts with the xenoliths (a) *Microgranodioritic host rock*. Note the porphyritic texture with phenocrysts of plagioclase, amphibole, biotite and quartz in a fine-grained matrix composed of quartz, plagioclase, K-feldspar and rare biotite. (b) *Ma3* Sharp contact, with a few xenocrysts of biotite from the xenolith in the host rock. (c) *Ma10* Sharp contact between xenolith and host rock underlined by a two mm large zone where abundant pinite replaces cordierite. (d, e) *Ma6* Host rock / xenolith contact underlined by the presence of large andalusite crystals sometimes fully enclosed in the host rock. (f) *Ma5* Host rock / xenolith contact marked a localized (<1 mm large) chloritized band. Mineral abbreviations from Whitney and Evans (2010).

Fig. 7 Major element characteristics of xenoliths and host rocks (a) Harker diagrams showing Al_2O_3, Na_2O+K_2O and TiO_2 variation as a function of SiO_2 (b) Cox classification diagram for plutonic rocks (Cox *et al*. 1979), plotted with GCDKit software (Janoušek *et al*., 2006). Note that sample Kar2b corresponds to the host rock of the corresponding studied xenolith.

Fig. 8 Trace element characteristics of xenoliths and host rocks (a) Harker diagrams showing selected transition element variation as a function of SiO_2. (b) La/Yb as a function of SiO_2.

Fig. 9 Spidergrams for xenoliths and host rocks (a) REE elements normalized to chondrite (Nakamura *et al.,* 1974) (b) Trace element spectra normalized to primitive mantle (McDonough and Sun, 1995). Diagrams plotted with GCDKit software (Janoušek *et al*., 2006)

Fig. 10 Pressure-temperature pseudosection for sample *Ma3*. Composition in weight percent from EDS mapping of the microdomain shown in Fig. 4g. Also shown are the relevant isopleths for plagioclase (X_{Ab}), garnet (X_{Alm}) and biotite (X_{Mg}, Ti-Bio pfu) corresponding to the observed compositions (Tables 2 and 4), and the upper stability of cordierite. Pressure-temperature field corresponding to the paragenesis observed in the microdomain is underlined in yellow. The suggested prograde and retrograde paths are indicated by white dashed arrows. Mineral abbreviations from Whitney and Evans (2010).

Fig. 11 Pressure-temperature pseudosection for sample *Ma10*. Composition in weight percent from whole-rock composition (Table 5). Also shown are the relevant isopleths for plagioclase

(X_{Ab}), garnet (X_{Alm}, X_{Grs}, X_{Prp}) and biotite (X_{Mg}^{Bt}) corresponding to the observed compositions (Tables 2 and 4), and the upper stability of cordierite. Pressure-temperature field corresponding to the paragenesis observed in the microdomain is underlined in yellow. The suggested prograde path is indicated by a white dashed arrow. Mineral abbreviations from Whitney and Evans (2010).

Fig. 12 Pressure-temperature pseudosection for sample *Ma6*. Composition in weight percent from EDS mapping of the microdomain shown in Fig. 4j. Also shown are the lower stability of garnet, the upper stability of K-feldspar and the solidus. Pressure-temperature field corresponding to the initial and final parageneses observed in the microdomain is underlined in yellow. Mineral abbreviations from Whitney and Evans (2010).

Fig. 13 Pressure-temperature pseudosection for sample *Kar2b*. Composition in weight percent from EDS mapping of the microdomain shown in Fig. 4k. Also shown are the lower stability of garnet, the upper stability of K-feldspar and the solidus. Pressure-temperature field corresponding to the initial and final parageneses observed in the microdomain is underlined in yellow. Mineral abbreviations from Whitney and Evans (2010).

Fig. 14 Pressure-temperature pseudosection for sample *Ma5*. Composition in weight percent from EDS mapping of the microdomain shown in Fig. 4l. Also shown is the lower stability of garnet. Pressure-temperature field corresponding to the assemblage observed in the microdomain is underlined in yellow. Mineral abbreviations from Whitney and Evans (2010).

Fig. 15. U-Th-Pb chemical ages of monazite for sample *Ma3*.

Fig. 16 Evolution of modal proportions of minerals from thermodynamic modeling. Cumulated modal proportion as a function of temperature for sample *Ma3* at 6 kbar (a) and 2.5 kbar (b) and for sample *Ma5* at 3 kbar (c). (d) Modal proportion of corundum as a fonction of T and $X(H_2O)$ in sample *Ma5*, with X=1 corresponding to 0.56 wt.% H_2O.

Fig. 17 Summary of pressure and temperature estimates for xenoliths of the Kariane locality. Pressure and temperature conditions for amphibolite to granulite facies Variscan metamorphism in Morocco estimated from previous work in regional metamorphism, contact metamorphism and in xenoliths from other localities are also shown. Position of the triple point for Al_2SiO_5 according to (HP) Holland and Powell (1998) or (P) Pattison (1992).

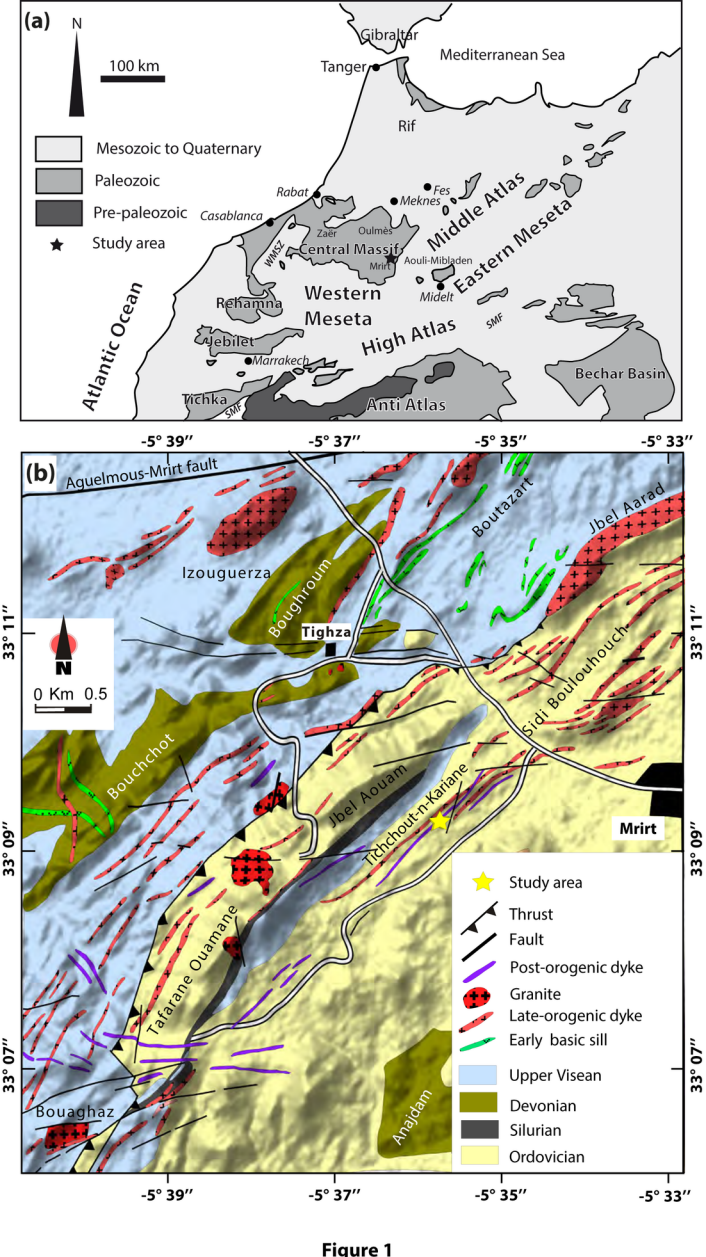

Figure 1

2-column fitting image

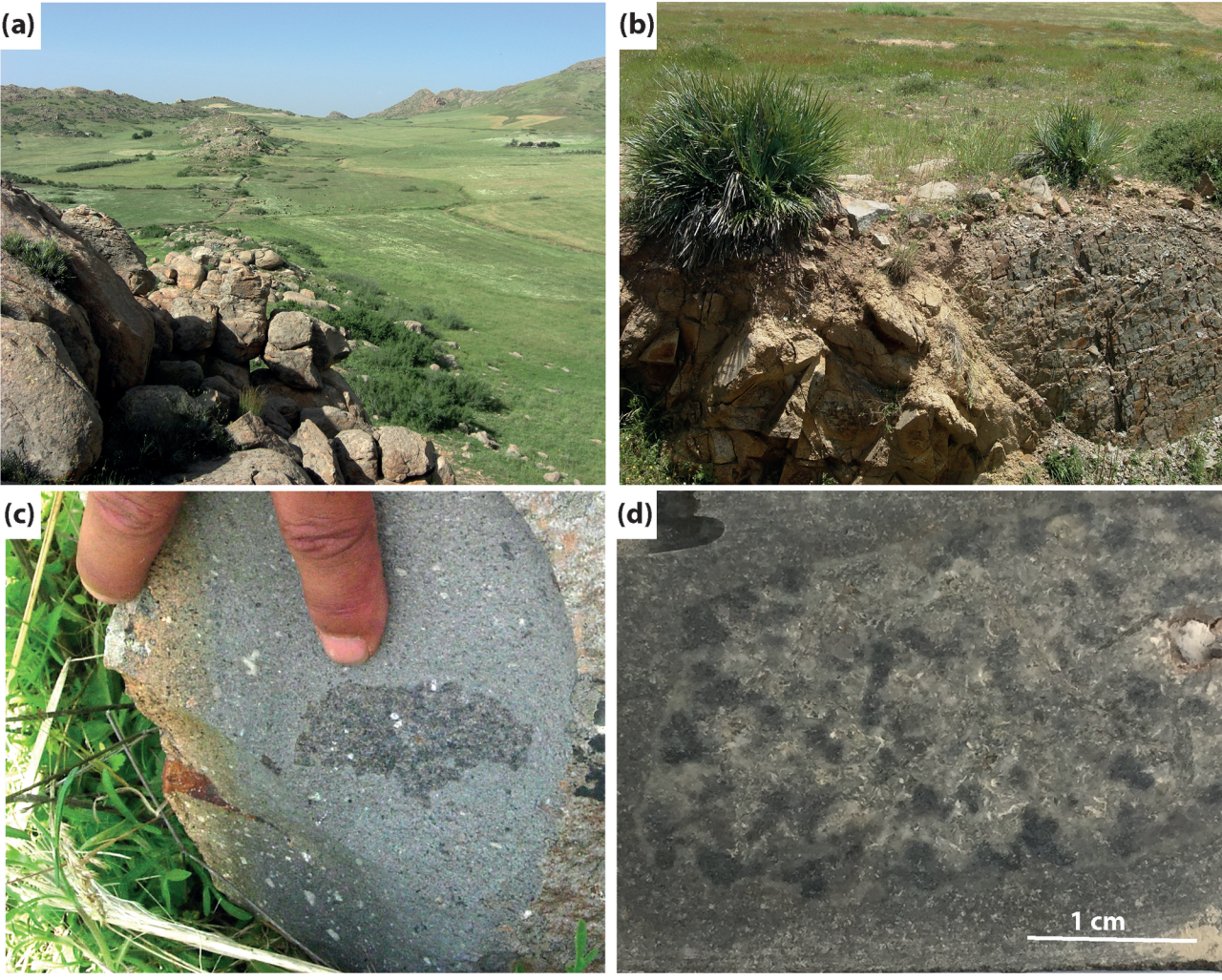

Figure 2

2-column fitting image

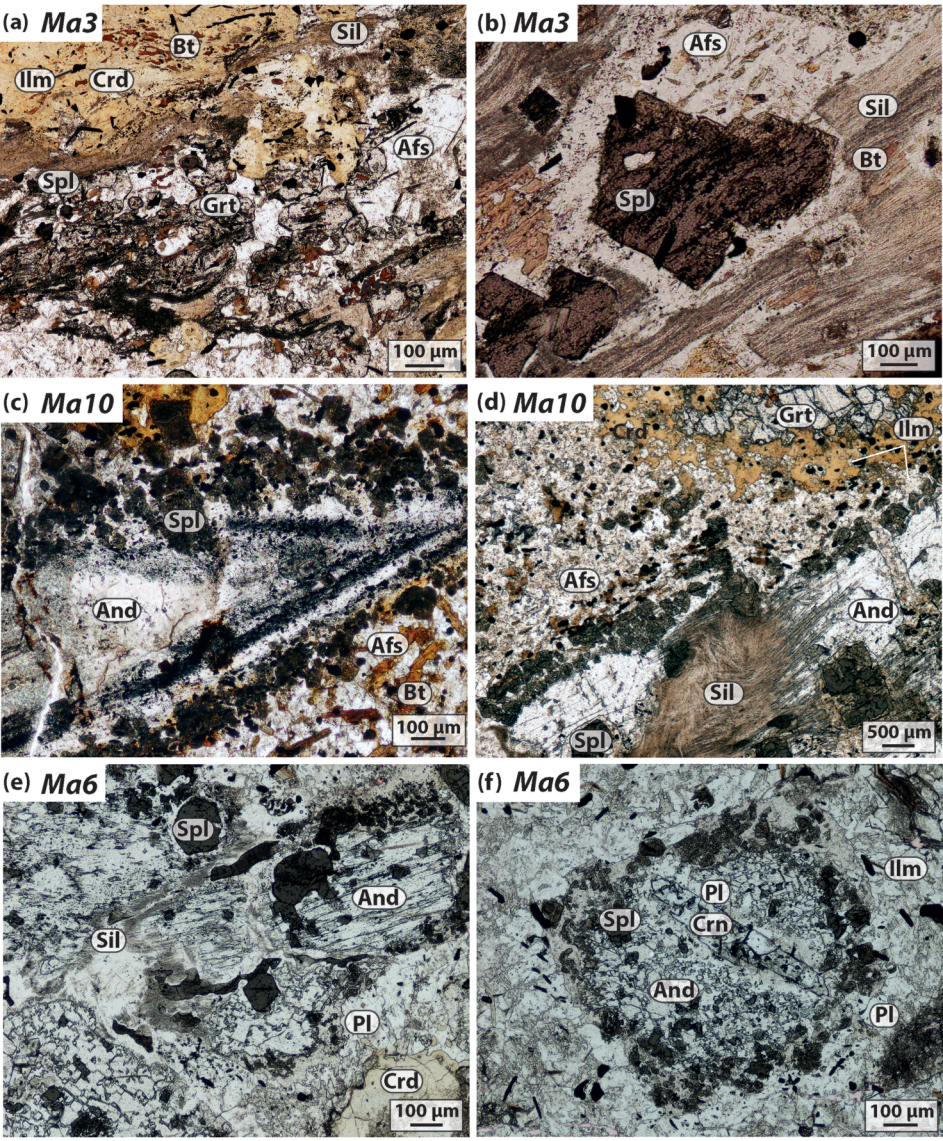

Figure 3

2-column fitting image

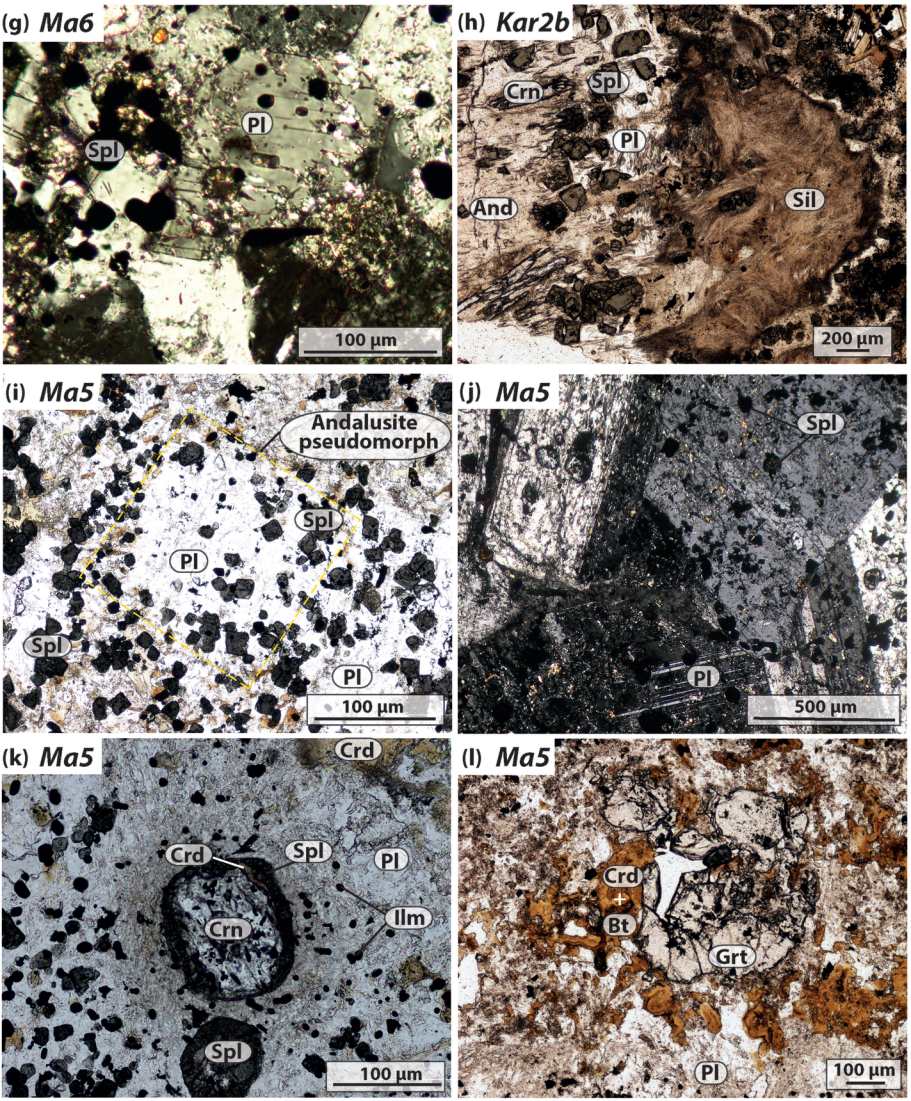

Figure 3 (continue)

2-column fitting image

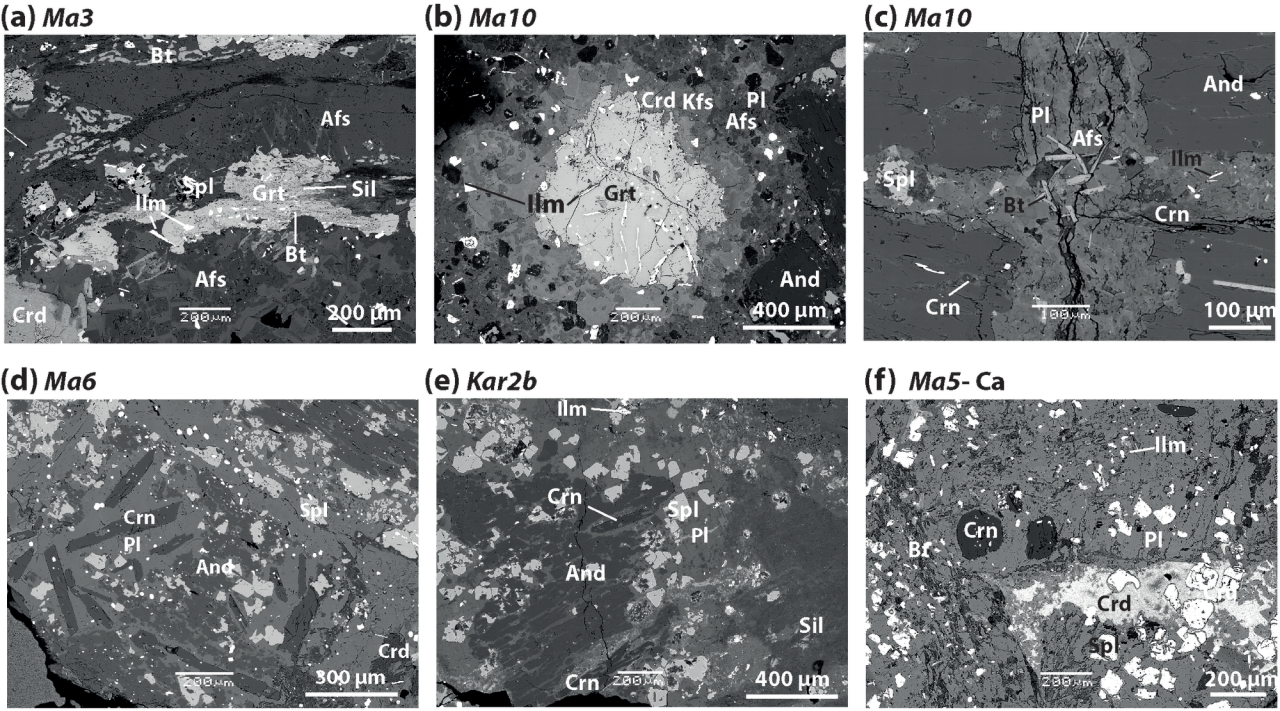

Figure 4

2-column fitting image

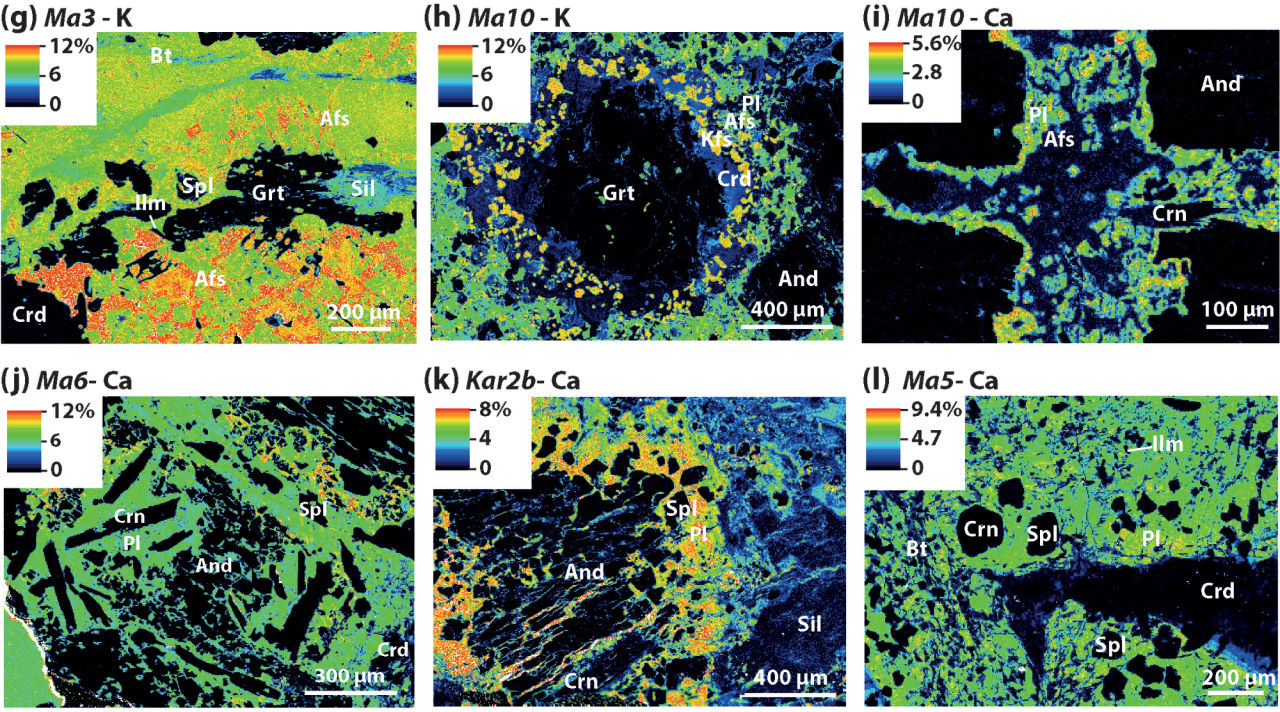

Figure 4 (continue)

2-column fitting image

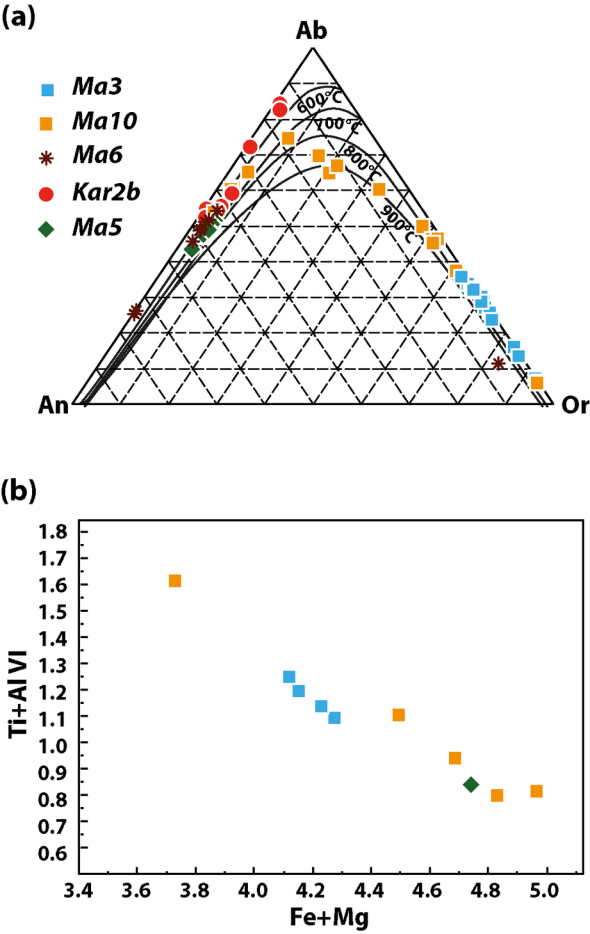

Figure 5

Single column fitting image

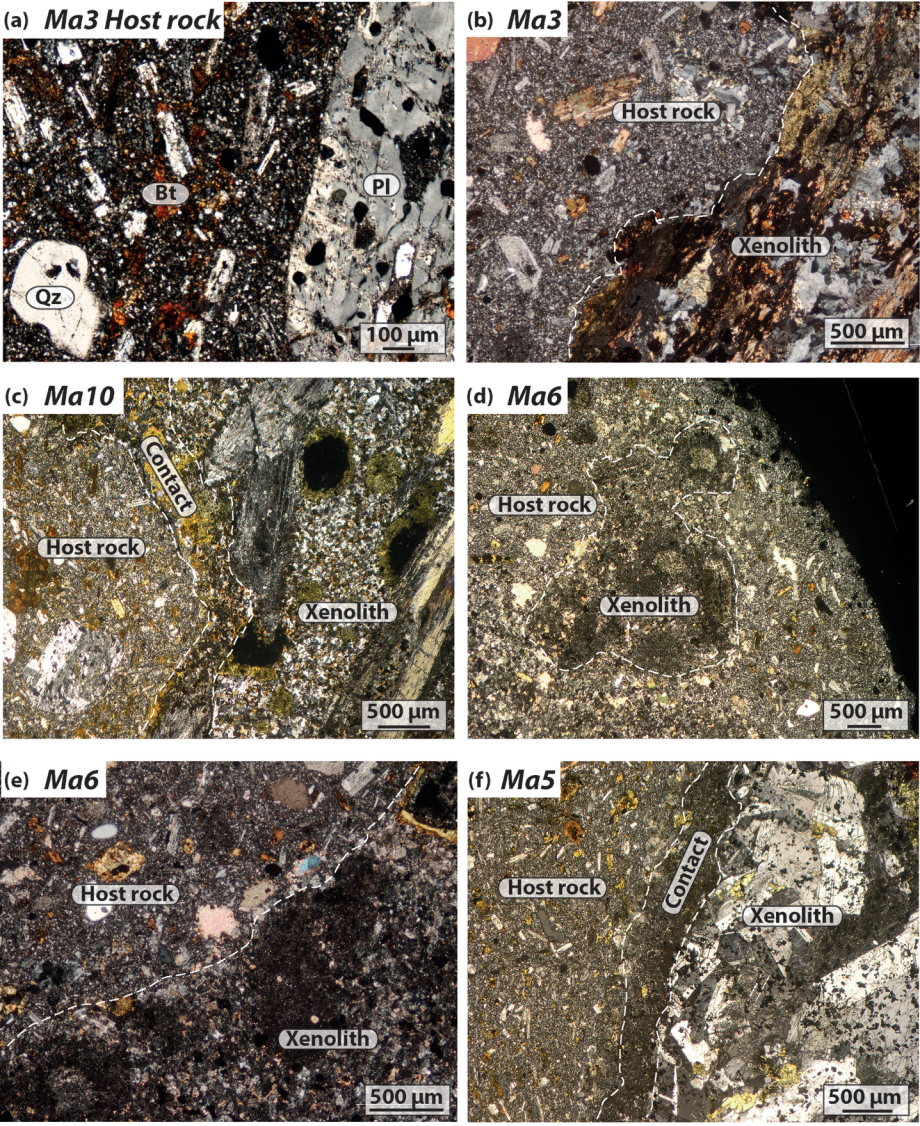

Figure 6

2-column fitting image

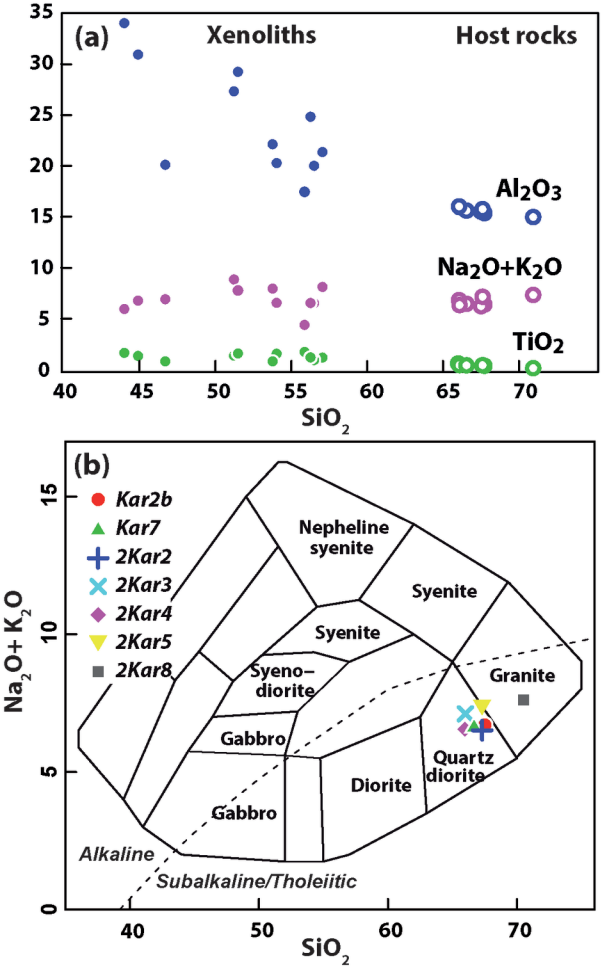

Figure 7

Single column fitting image

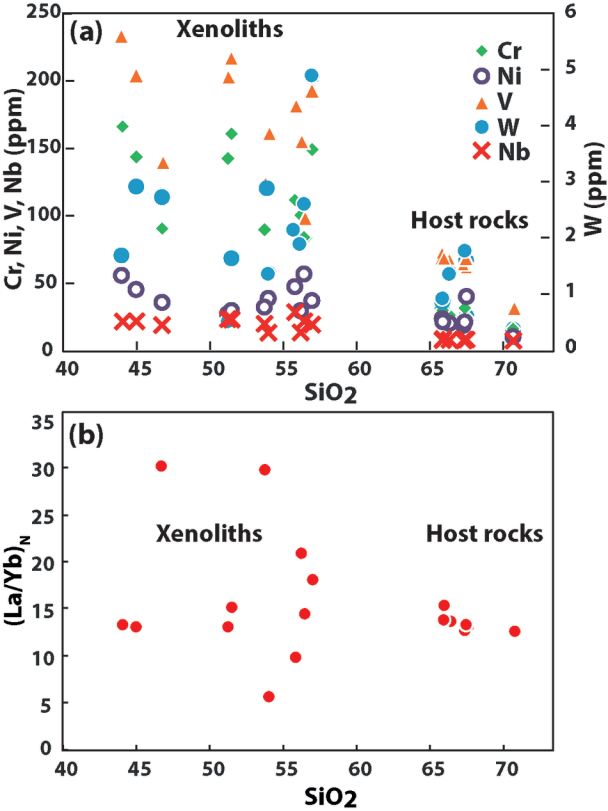

Figure 8

Single column fitting image

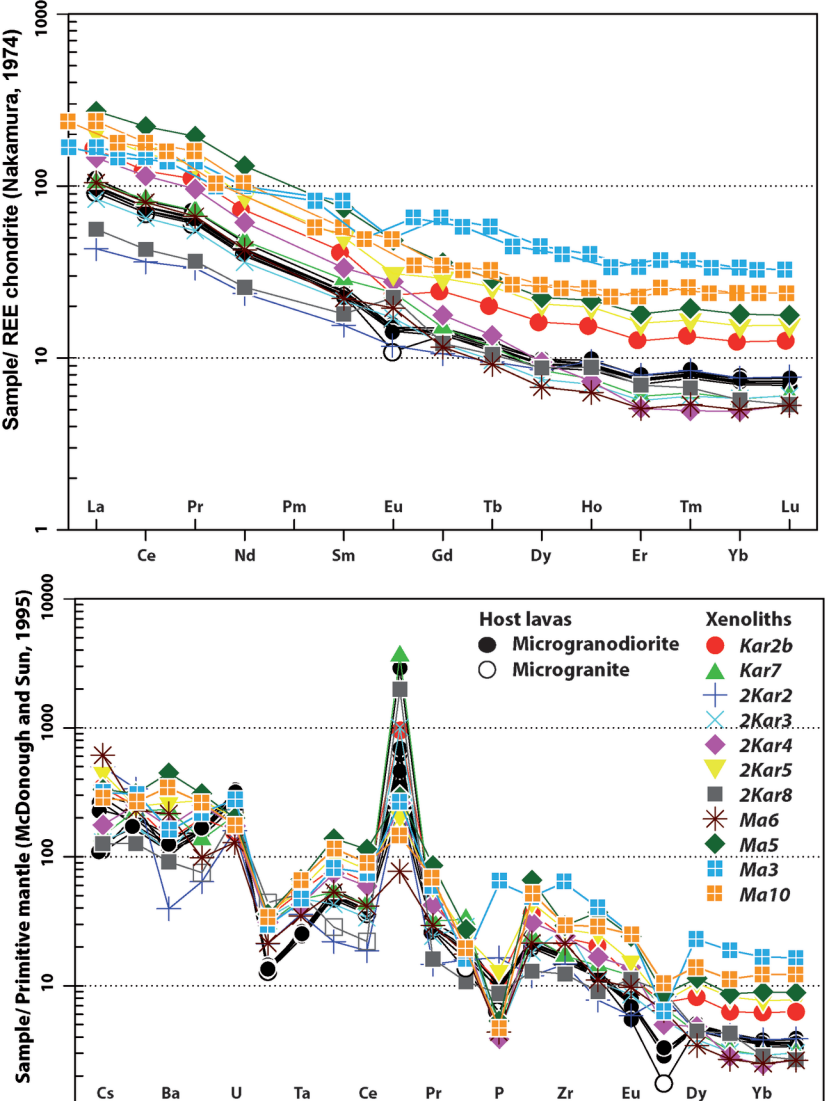

Figure 9

2-column fitting image

Sample *Ma3* (Microdomain)

SiO_2 55.40, TiO_2 1.22, Al_2O_3 21.07, FeO 7.85, MnO 0.14, MgO 1.85, CaO 0.41, Na_2O 1.64, K_2O 9.46, H_2O 0.95

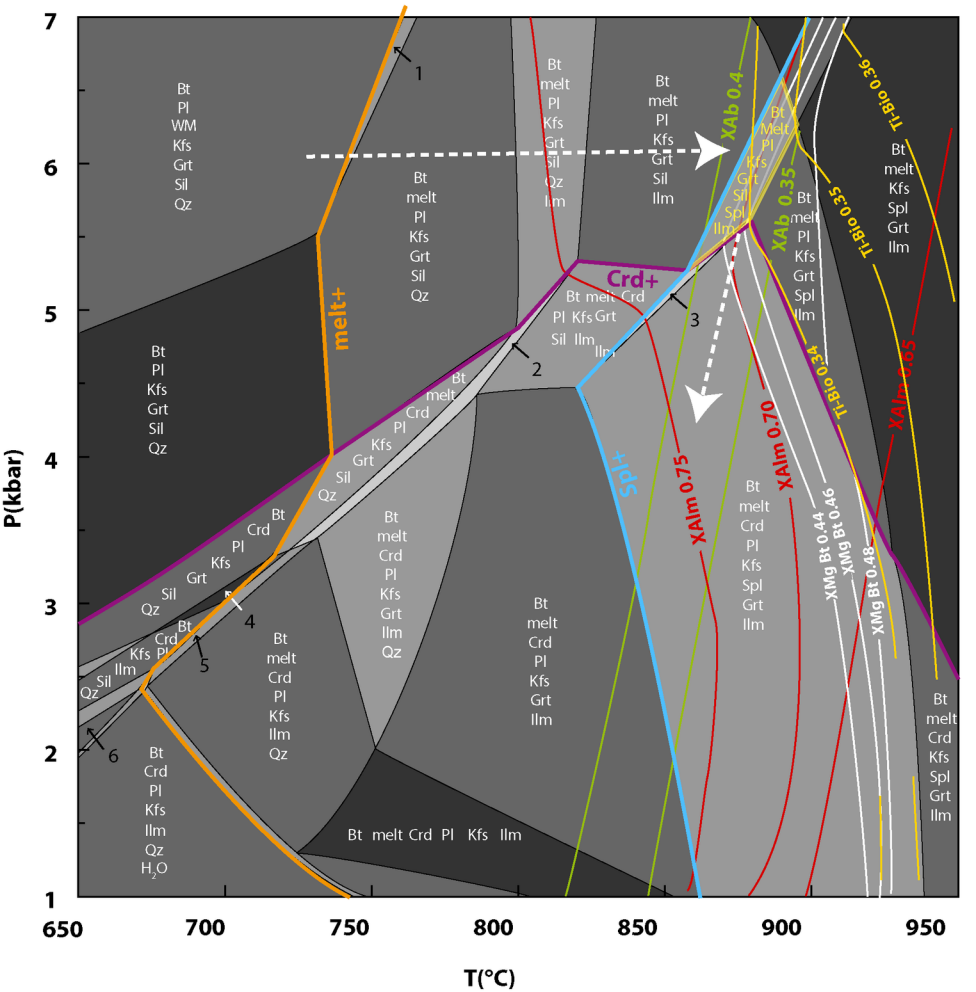

Additional fields

1. Bt melt WM Pl Kfs Grt Sil Qz	2. Bt melt Crd Pl Kfs Grt Sil Ilm	3. Bt melt Crd Pl Kfs Spl Grt Sil Ilm
4. Bt Crd Pl Kfs Ilm Sil Qz	5. Bt melt Crd Pl Kfs Ilm Sil Qz	6. Bt WM Crd Pl Kfs Ilm Qz

Figure 10

2-column fitting image

Sample *Ma10* (Whole-rock)

SiO_2 46.20; TiO_2 2.08; Al_2O_3 35.47; FeO 6.50; MnO 0.13; MgO 1.81; CaO 0.70; Na_2O 2.03; K_2O 4.52; H_2O 0.54

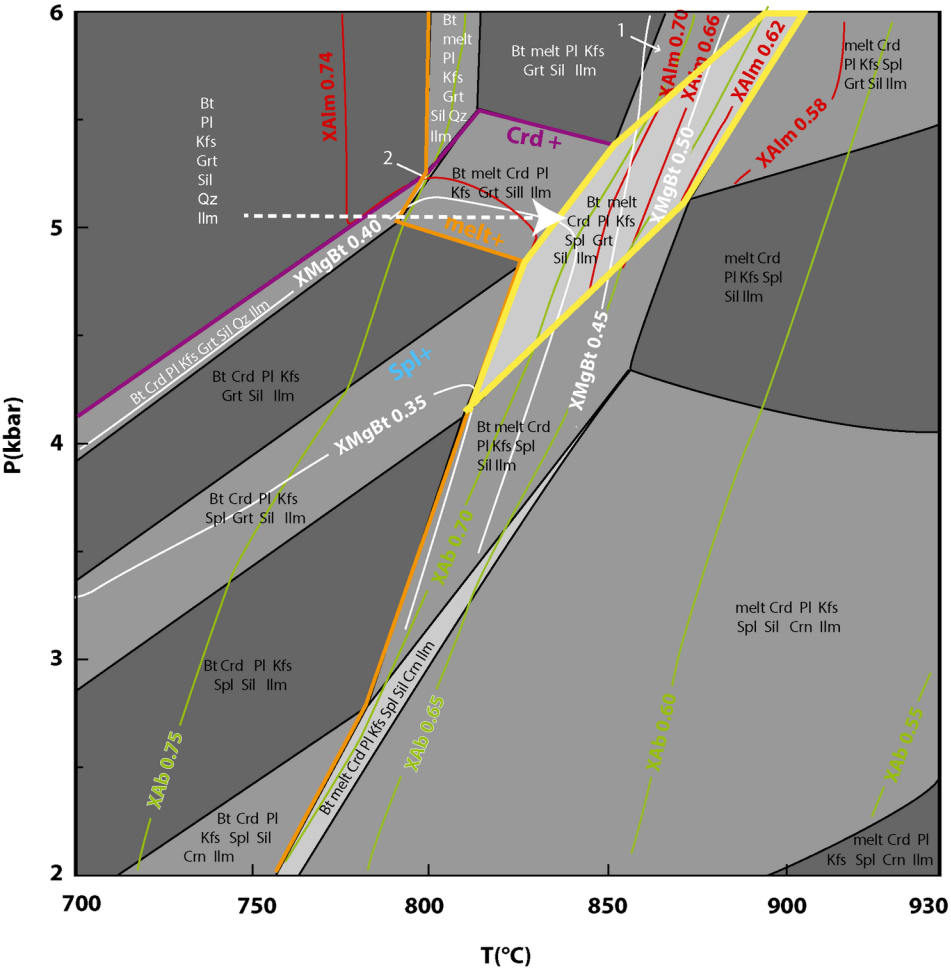

Additional fields

1. Bt melt Pl Kfs Spl Grt Sil Ilm
2. Bt melt Crd Pl Kfs Grt Sil Qz Ilm

Figure 11

2-column fitting image

Sample *Ma6* (Microdomain)

SiO_2 38.72; TiO_2 1.06; Al_2O_3 45.69; FeO 5.25; MnO 0.06; MgO 1.06; CaO 5.14; Na_2O 2.37; K_2O 0.65; H_2O 0.1

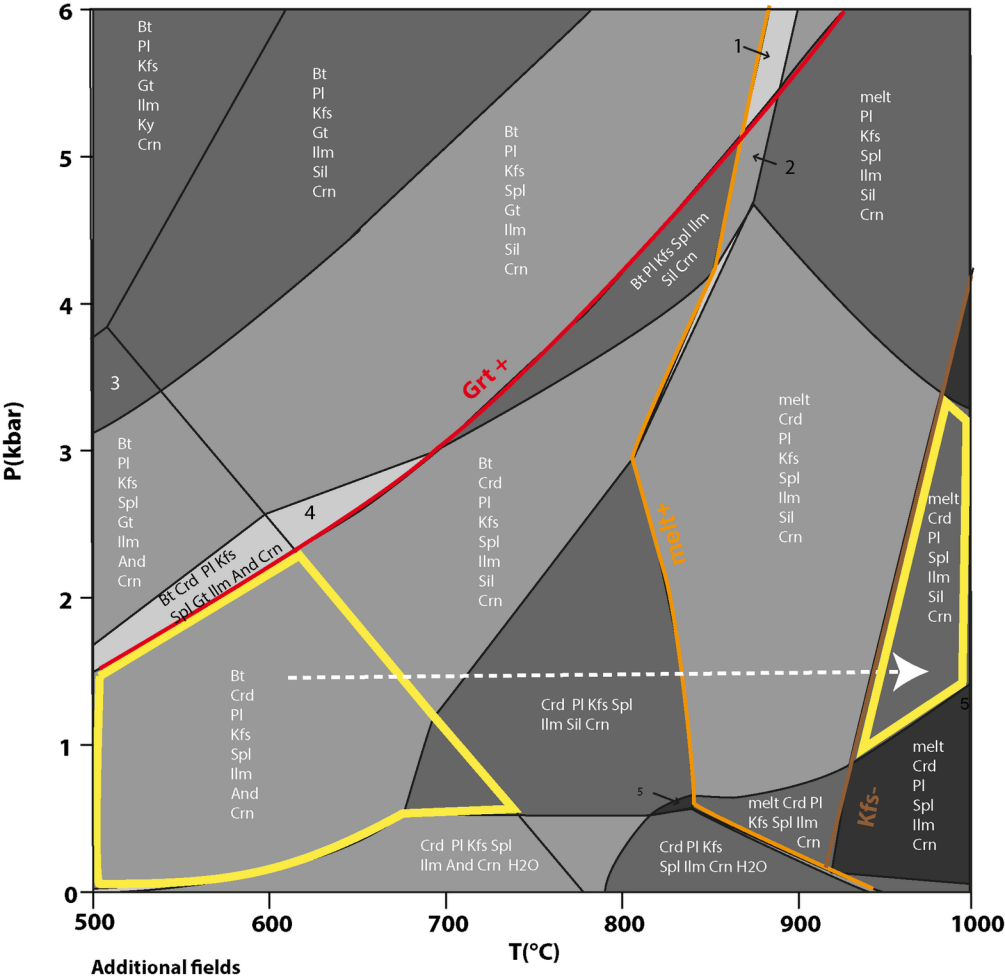

Additional fields

1 Bt melt Pl Kfs Spl Gt Ilm Sil Crn	2 Bt melt Pl Kfs Spl Ilm Sil Crn	3 Bt Pl Kfs Gt Ilm And Crn
4 Bt Crd Pl Kfs Spl Grt Ilm Sil Crn	5 Crd Pl Kfs Spl Grt Ilm Crn	

Figure 12

2-column fitting image

Sample *Kar2b* (Microdomain)

SiO_2 35.76; TiO_2 0.32; Al_2O_3 49.11; FeO 6.46; MnO 0.07; MgO 1.75; CaO 3.17; Na_2O 1.71; K_2O 0.19; H_2O 0.14

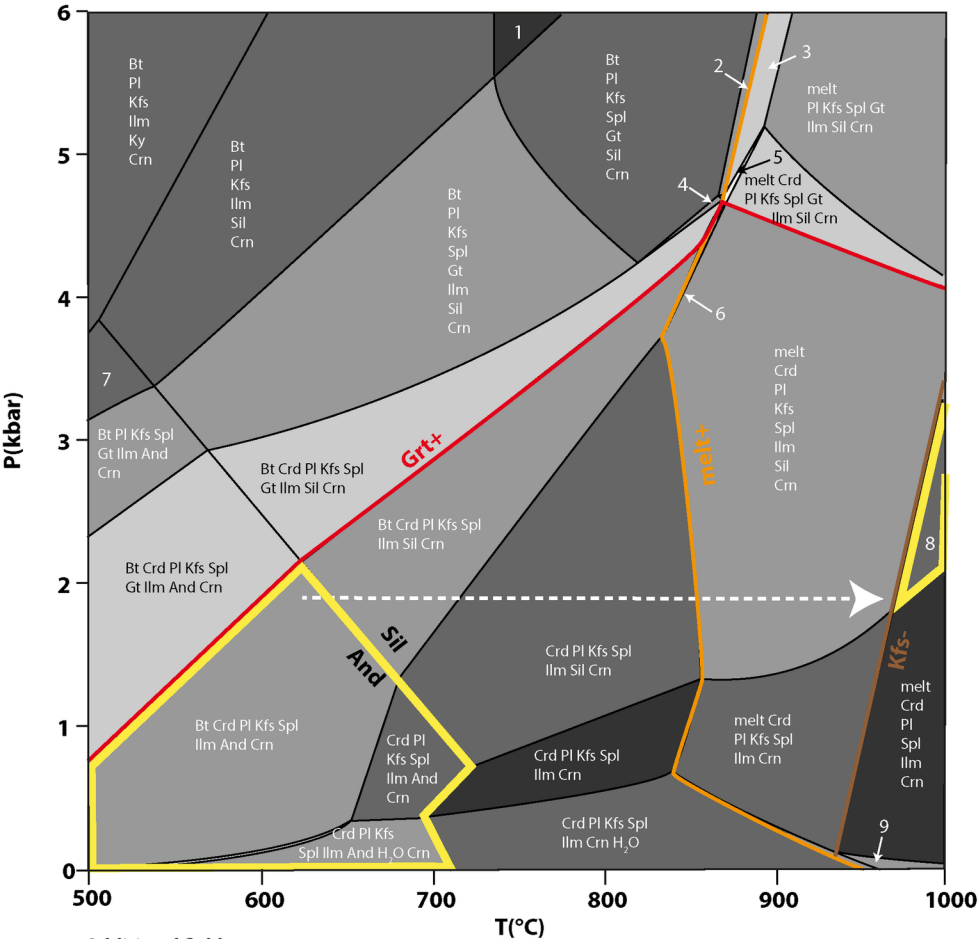

Additional fields

1 - Bt Pl Kfs Gt Sil Crn	2 - Bt melt Pl Kfs Spl Gt Sil Crn	3 - Bt melt Pl Kfs Spl Gt Ilm Sil Crn
4 - Bt Crd Pl Kfs Spl Gt Sil Crn	5 - Bt melt Crd Pl Kfs Spl Gt Sil Crn	6 - Bt melt Crd Pl Kfs Spl Ilm Sil Crn
7 –Bt Pl Kfs Gt Ilm And Crn	8 - melt Crd Pl Spl Ilm Sil Crn	9 - melt Crd Pl Spl Ilm Crn H_2O

Figure 13

2-column fitting image

Sample *Ma5* (Microdomain)

SiO_2 46.84; TiO_2 1.44; Al_2O_3 32.11; FeO 5.73; MnO 0.10; MgO 2.18; CaO 5.34; Na_2O 3.95; K_2O 1.77; H_2O 0.53

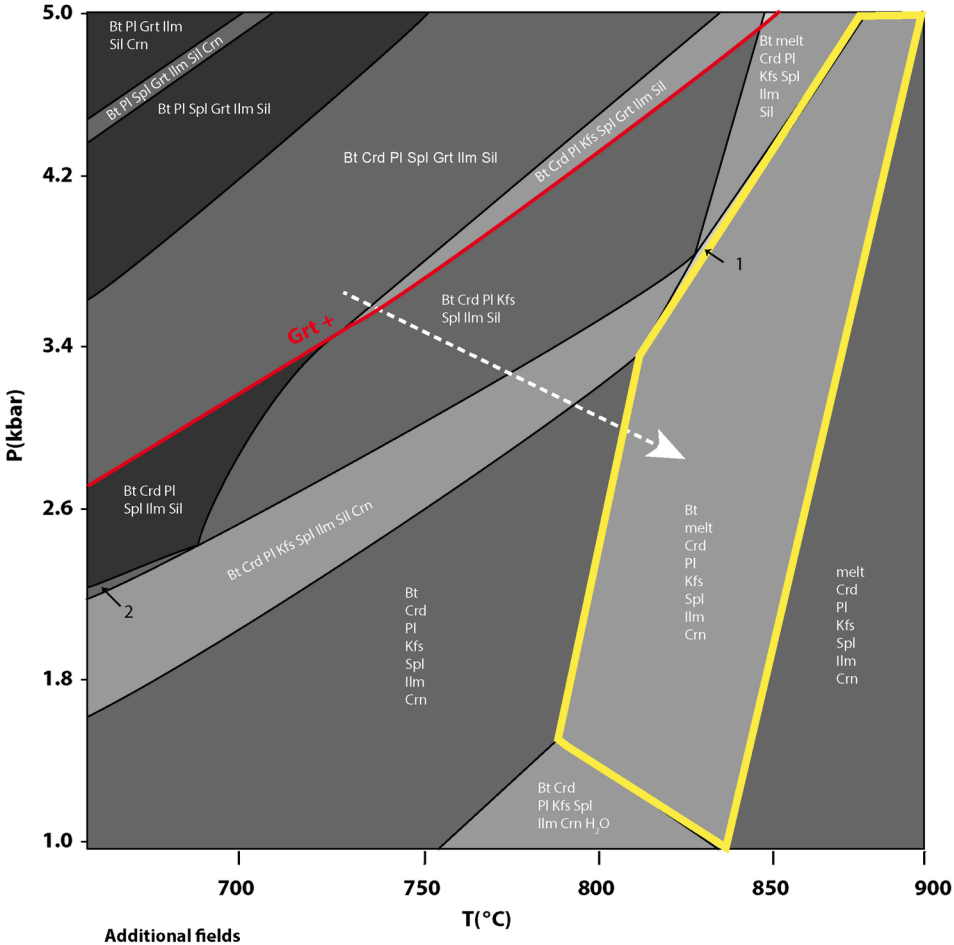

Additional fields

1 - Bt melt Crd Pl Kfs Spl Ilm Sil Crn

2 - Bt Crd Pl Spl Ilm Sil Crn

Figure 14

2-column fitting image

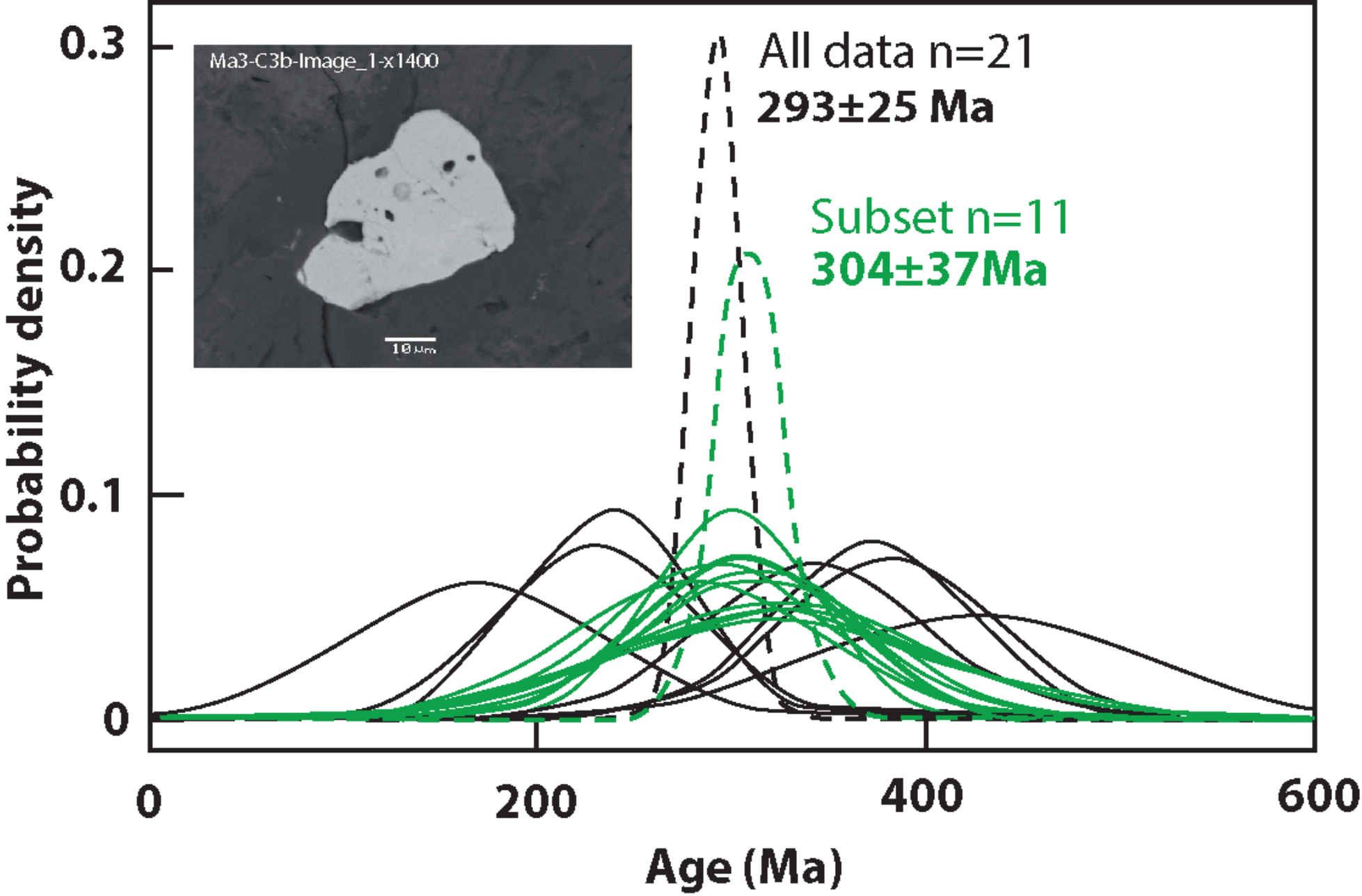

Figure 15

Single column fitting image

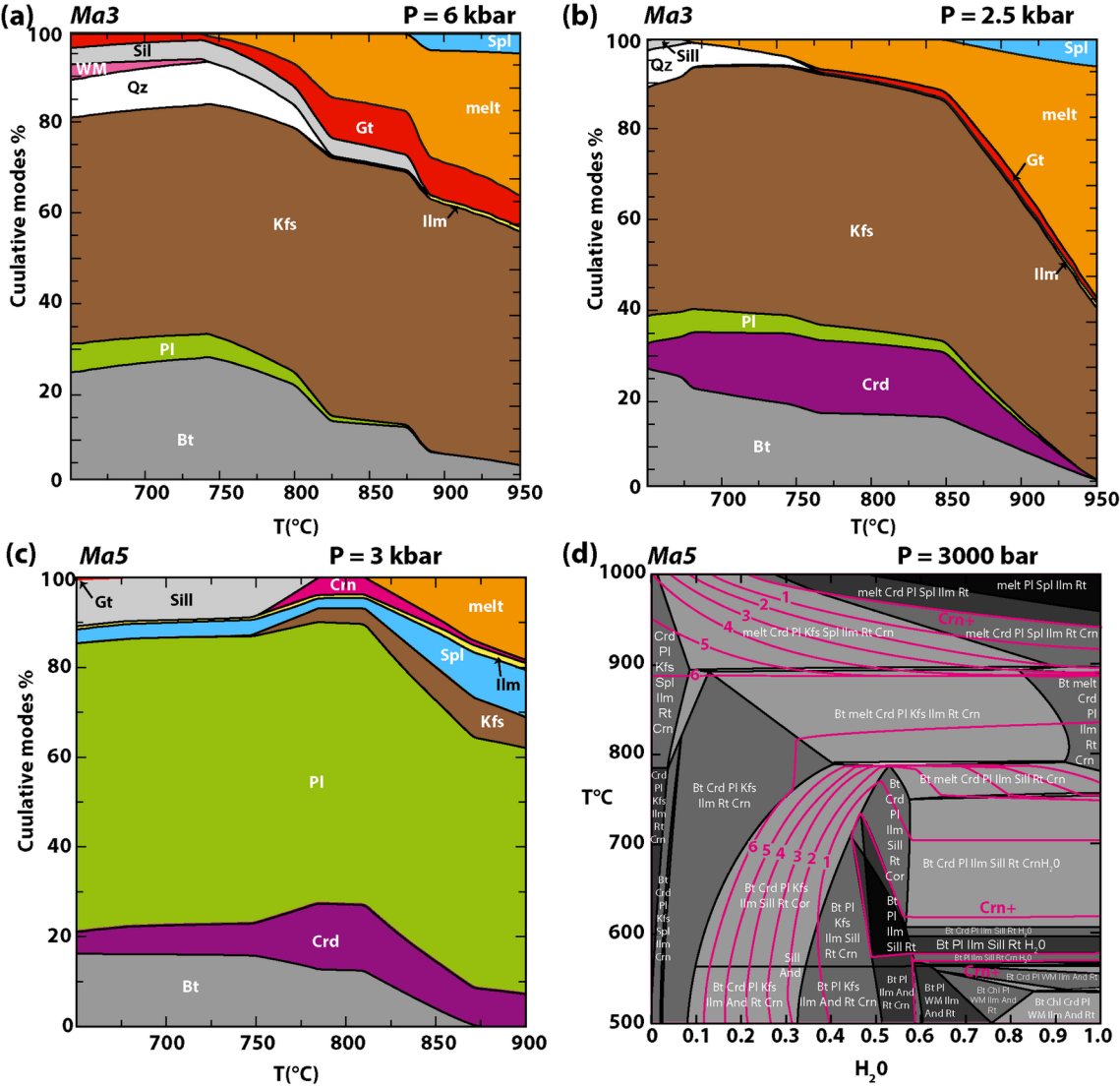

Figure 16

2-column fitting image

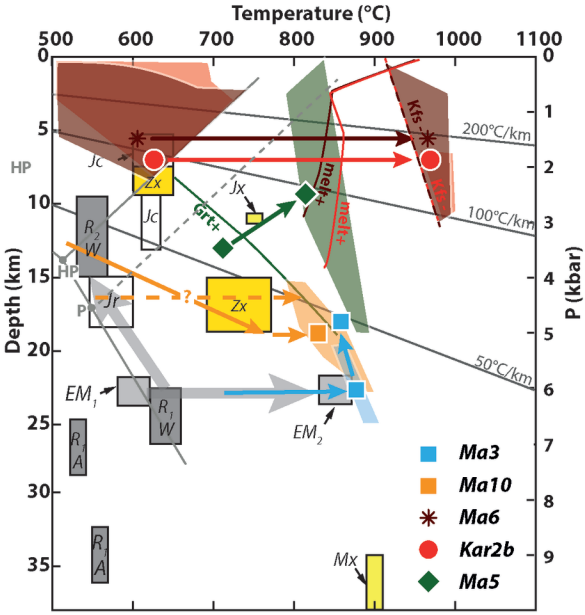

R — *Rehamna.*
Metamorphic condition : peak pressure (1) and exhumation (2) from Aghzer et Arenas (1998) (A) and Wernert et al. (2016) (W).

J — *Jebilet.*
Regional (*r*) or contact (*c*) metamorphic conditions from Delchini et al. (2016)

EM — *Eastern Moulouya.*
Regional metamorphic conditions (1) and peak temperature due to magma injection (2) from Elabouyi et al. (2019)

Zx — *Zaër pluton.*
Metamorphic conditions in xenoliths, from Haïmeur et al. (2003)

Jx — *Oulad Ouaslam granite (Jebilet).*
Metamorphic conditions in xenoliths, from Bouloton et al. (1991)

Mx — *Quaternary basalts (Middle Atlas).*
Granulitic xenoliths, from Moukadiri and Bouloton (1998)

Figure 17

Single column fitting image

Table 1

Summary of petrological description of xenoliths

	Ma3	*Ma10*	*Ma6 and Kar2b*	*Ma 5*
	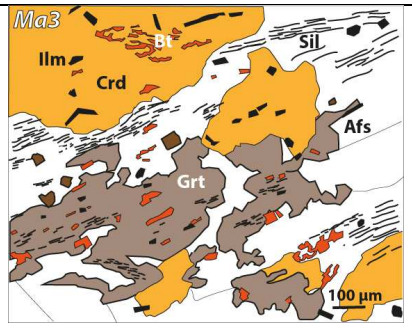	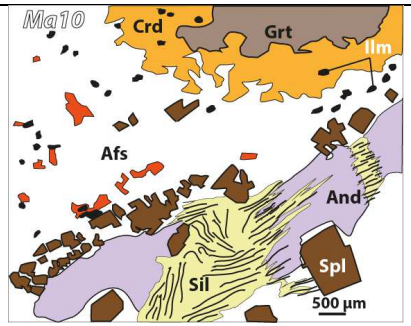	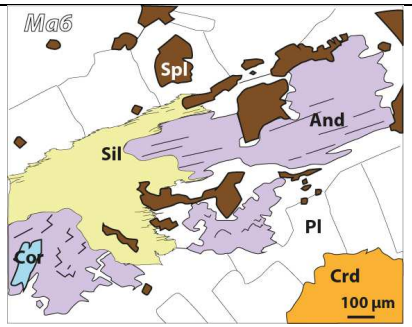	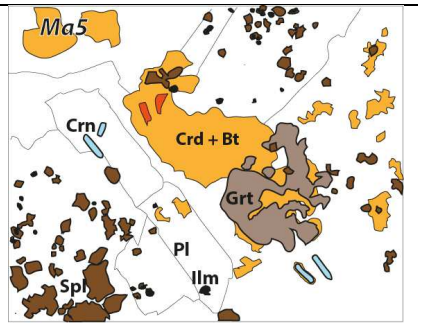
Xenolith chemistry	SiO_2 46.76 % Al_2O_3 20.26 % ΣREE 1317 ppm	SiO_2 44.07 % Al_2O_3 33.84 % ΣREE 1297 ppm	SiO_2 56.24 % (*Ma6*) 44.99 % (*Kar2b*) Al_2O_3 24.91 % (Ma6) 30.99 % (*Kar2b*) ΣREE 522 ppm (*Ma6*) 873 ppm (*Kar2b*)	SiO_2 44.99 % Al_2O_3 30.99 % ΣREE 1495 ppm
Pre-entrapment metamorphism remnants	Biotite, sillimanite, garnet	Andalusite, garnet	Andalusite, corundum	Garnet, corundum, biotite, ilmenite
Contact metamorphism	Garnet, spinel, alkali feldspar, biotite, ilmenite, melt Late cordierite, K-feldspar	Plagioclase, alkali feldspar, biotite, spinel, ilmenite, sillimanite, cordierite, melt	Spinel, plagioclase, biotite, sillimanite, cordierite, melt	Spinel, cordierite, corundum, ilmenite, plagioclase, Afs, melt
Mineral chemistry	Afs Or 62-90 Spl X_{Fe} 0.67-0.72 Grt X_{Alm} 0.64-0.73 Bt X_{Mg} 0.45 TiO_2 6-8%	Pl An 35-45 Afs Or 47-92 Spl X_{Fe} 0.63-0.79 Grt X_{Alm} 0.59-0.67 Bt X_{Mg} 0.4-0.56 TiO_2 3-7%	Pl An26-74 (*Ma6*) An15-45 (*Kar2b*) Afs Or 57-88 Spl X_{Fe} 0.64-0.69 (*Ma6*) X_{Fe} 0.70-0.74 (*Kar2b*)	Pl An 45-53 Spl X_{Fe} 0.57-0.64 Bt X_{Mg} 0.49-0.56 TiO_2 < 5%
Contact *P-T* conditions	*P* > 5 kbar *T* 850-900°C	*P* 4-6 kbar *T* 850 °C	*P* < 2 kbar *T* > 900 °C	*P* < 5 kbar *T* 800-850 °C

Table 2

Representative electron microprobe analyses of feldspars in xenoliths

	Ma3	*Ma3*	*Ma3*	*Ma10*	*Ma10*	*Ma10*	*Ma6*	*Ma6*	*Ma6*	*Kar2b*	*Kar2b*	*Kar2b*	*Ma5*	*Ma5*	*Ma5*
SiO_2	66.03	64.78	64.52	55.72	63.49	65.32	54.02	65.8	59.23	65.9	57.77	62.1	57.12	55.09	55.97
TiO_2	0.00	0.28	0.06	0.03	0.11	0.00	0.00	0.07	0.00	0.09	0.18	0.14	0.03	0.06	0.02
Al_2O_3	18.8	18.9	18.87	28.71	19.21	22.10	29.25	18.37	25.49	22.13	26.6	24.39	27.00	28.62	27.89
Fe_2O_3	0.1	0.11	0.02	0.25	1.56	0.00	0.25	0.06	0.22	0.38	0.50	0.13	0.12	0.18	0.10
CaO	0.31	0.00	0.16	9.24	0.07	3.03	11.44	0.2	5.39	3.28	8.93	5.83	9.23	11.05	10.13
Na_2O	4.2	0.74	3.24	6.31	0.61	8.98	4.70	2.89	7.71	10.24	6.26	8.53	5.93	5.02	5.52
K_2O	10.93	15.32	11.73	0.46	14.35	1.21	0.34	12.55	1.02	0.20	0.57	0.19	0.65	0.49	0.59
Total	100.36	102.32	98.62	100.73	100.31	100.64	100.01	99.94	99.19	102.23	100.9	101.4	100.08	100.50	100.23
Si	2.99	2.99	3.03	2.58	2.96	3.01	2.51	3.05	2.79	3.01	2.67	2.86	2.65	2.55	2.59
Al	1.00	1.03	1.05	1.57	1.06	1.20	1.60	1.00	1.41	1.19	1.45	1.32	1.48	1.56	1.52
Ti	0.00	0.01	0.00	0.00	0.00	0.00	0.00	0.00	0.00	0.00	0.01	0.00	0.00	0.00	0.00
Fe^{2+}	0.00	0.00	0.00	0.01	0.05	0.00	0.01	0.00	0.01	0.01	0.02	0.00	0.00	0.01	0.00
Ca	0.02	0.00	0.01	0.46	0.00	0.15	0.57	0.01	0.27	0.16	0.44	0.29	0.46	0.55	0.50
Na	0.37	0.00	0.00	0.00	0.00	0.00	0.00	0.00	0.00	0.00	0.00	0.00	0.00	0.00	0.00
K	0.63	0.90	0.70	0.03	0.85	0.07	0.02	0.74	0.06	0.01	0.03	0.01	0.04	0.03	0.03
Ab	36.32	6.84	29.33	53.84	6.05	78.42	41.79	25.67	67.87	84.04	54.11	71.82	51.75	43.85	47.97
An	1.48	0.00	0.80	43.57	0.38	14.62	56.22	0.98	26.22	14.88	42.65	27.13	44.52	53.34	48.65
Or	62.20	93.16	69.87	2.58	93.57	6.95	1.99	73.35	5.91	1 .08	3.24	1.05	3.72	2.82	3.37

Chemical formulae were calculated on the basis of 8 oxygens

Table 3

Representative electron microprobe analyses of spinel in xenoliths

	Ma3	*Ma3*	*Ma10*	*Ma10*	*Ma6*	*Ma6*	*Kar2b*	*Kar2b*	*Ma5*	*Ma5*
SiO_2	0.13	0.05	0.08	0.21	0.22	0.15	0.19	0.03	0.04	0.19
TiO_2	0.21	0.26	0.34	0.36	0.14	0.19	0.32	0.37	0.21	0.42
Al_2O_3	60.01	59.23	61.14	62.47	59.38	60.64	60.43	60.57	60.51	60.84
Cr_2O_3	0.04	0.13	0.07	0.17	0.04	0.06	0.03	0.04	0.17	0.09
Fe_2O_3	1.00	2.51	1.05	0.00	0.92	0.00	0.93	0.96	1.48	0.21
FeO	29.31	29.04	27.84	29.59	31.52	29.59	30.08	27.87	24.66	27.98
MnO	0.00	0.04	0.25	0.24	0.27	0.34	0.53	0.40	0.20	0.23
MgO	7.72	7.88	9.05	8.47	6.32	7.22	7.43	8.76	10.56	8.80
ZnO	0.00	0.00	0.11	0.15	0.00	0.53	0.22	0.00	0.07	0.33
Total	98.42	99.14	99.93	101.66	98.81	98.72	100.15	99.00	97.90	99.09
Si	0.00	0.00	0.00	0.01	0.01	0.00	0.01	0.00	0.01	0.00
Ti	0.01	0.01	0.01	0.01	0.00	0.00	0.01	0.01	0.01	0.01
Al VI	1.97	1.93	1.96	1.97	1.96	1.97	1.96	1.96	1.96	1.96
Cr	0.00	0.00	0.00	0.00	0.00	0.00	0.00	0.00	0.00	0.00
Fe^{3+}	0.02	0.05	0.02	0.00	0.02	0.01	0.02	0.02	0.02	0.02
Fe^{2+}	0.68	0.67	0.63	0.66	0.74	0.69	0.69	0.64	0.69	0.64
Mn^{2+}	0.00	0.00	0.01	0.01	0.01	0.01	0.01	0.01	0.01	0.01
Mg	0.32	0.33	0.37	0.34	0.26	0.30	0.30	0.36	0.30	0.36
Zn	0.00	0.00	0.00	0.00	0.00	0.01	0.00	0.00	0.00	0.00
XFe^{2+}	0.68	0.67	0.63	0.66	0.74	0.70	0.69	0.64	0.69	0.64

Chemical formulae were calculated on the basis of 4 oxygens

Table 4

Representative electron microprobe analyses of garnet and biotite in xenoliths

	Garnet					Biotite						
	Ma3	*Ma3*	*Ma10*	*Ma10*		*Ma3*	*Ma3*	*Ma3*	*Ma10*	*Ma5*	*Ma5*	*Ma5*
SiO_2	39.00	37.45	37.94	37.23	SiO_2	34.62	36.23	34.67	36.05	35.4	35.17	36.17
TiO_2	0.21	0.18	0.14	0.39	TiO_2	7.98	6.21	8.14	4.29	5.15	3.77	4.91
Al_2O_3	21.98	20.88	22.4	21.04	Al_2O_3	17.33	16.18	16.71	16.81	15.56	17.15	15.71
Cr_2O_3	0.09	0.00	0.00	0.00	Cr_2O_3	0.01	0.18	0.3	0.06	0	0.02	0.08
Fe_2O_3(c)	0.19	0.91	1.49	1.06	FeO	16.87	18.45	17.68	17.23	18.81	17.35	18.13
FeO	30.37	32.61	26.85	31.05	MnO	0.07	0.09	0	0.21	0.02	0	0.1
MnO	0.57	0.35	1.60	2.69	MgO	8.8	8.6	8.89	11.12	10.19	12.28	11.34
MgO	8.62	6.14	8.57	5.86	CaO	0	0.03	0.06	0.02	0	0.1	0.15
CaO	0.4	0.81	1.36	1.32	Na2O	0.37	0.45	0.44	0.47	0.56	0.5	0.43
Total	101.42	99.33	100.35	99.66	K2O	8.78	8.98	8.71	8.28	8.99	8.27	8.41
					BaO	0.11	0.18	0.23	0.47	0	0.6	0.35
Si	2.99	2.98	2.93	2.96	NiO	0.04	0	0.06	0	0.04	0.08	0
Ti	0.01	0.01	0.01	0.02	F	1.24	1.28	1.76	1.22	2.64	1.93	2.02
Al IV	0.01	0.02	0.07	0.04	Cl	0.15	0.25	0.16	0.28	0.78	0.21	0.65
Al VI	1.97	1.94	1.97	1.93	Total	96.37	97.11	97.81	96.51	98.14	97.43	98.45
Cr	0.01	0.00	0.00	0.00								
Fe^{3+}	0.01	0.05	0.09	0.06	Si	2.585	2.703	2.566	2.686	2.629	2.604	2.660
Fe^{2+}	1.95	2.17	1.73	2.00	Ti	0.448	0.349	0.453	0.240	0.288	0.210	0.272
Mn^{2+}	0.04	0.02	0.11	0.18	Al IV	1.415	1.297	1.434	1.314	1.362	1.396	1.340
Mg	0.98	0.73	0.99	0.69	Al VI	0.110	0.125	0.024	0.163	0.000	0.101	0.022
Ca	0.03	0.07	0.11	0.11	Fe^{2+}	1.054	1.151	1.094	1.074	1.168	1.074	1.115
					Mn^{2+}	0.004	0.006	0.000	0.013	0.001	0.000	0.006
Pyrope	32.80	24.00	33.59	23.00	Mg	0.980	0.956	0.981	1.235	1.128	1.355	1.243
Almandin	64.87	73.00	59.02	67.00	Ca	0.000	0.002	0.005	0.002	0.000	0.008	0.012
Spessartine	1.24	1.00	3.56	6.00	Na	0.054	0.065	0.063	0.068	0.081	0.072	0.061
Andradite	0.54	0.00	3.83	0.00	K	0.836	0.855	0.822	0.787	0.852	0.781	0.789
Uvarovite	0.27	0.00	0.00	0.00	Ba	0.003	0.005	0.007	0.014	0.000	0.017	0.010
Grossulaire	0.29	2.00	0.00	4.00	Ni	0.002	0.000	0.004	0.000	0.002	0.005	0.000
XMg	0.34	0.26	0.36	0.24	F	0.293	0.302	0.412	0.287	0.620	0.452	0.470
					Cl	0.019	0.032	0.020	0.035	0.098	0.026	0.081
					XMg	0.482	0.454	0.473	0.559	0.491	0.558	0.527

Chemical formulae were calculated on the basis of 12 oxygens for garnet and 11 oxygens for biotite

Table 5

Whole rock analyses of selected host rocks and xenoliths (Major elements in wt.%, trace elements in ppm)

	Host rocks		Xenoliths										
	Kar2b	2Kar8	Kar2b	Kar 7	2Kar 2	2Kar 3	2Kar 4	2Kar 5	2Kar 8	Ma6	Ma5	Ma3	Ma10
SiO_2	67.58	70.76	44.99	57.01	54.03	56.47	53.76	51.25	55.84	56.24	51.51	46.76	44.07
Al_2O_3	15.49	15.11	30.99	21.46	20.39	20.12	22.22	27.39	17.58	24.91	29.29	20.26	33.84
Fe_2O_3	5.15	2.74	9.41	6.22	8.75	8.98	8.08	5.92	12.66	5.31	6.01	9.55	6.20
MnO	0.22	0.04	0.25	0.24	0.16	0.18	0.10	0.15	0.12	0.11	0.22	0.15	0.13
MgO	1.82	1.00	2.67	2.37	3.17	4.33	2.55	2.26	4.15	1.78	1.57	3.31	1.74
CaO	2.37	2.34	2.94	2.88	4.62	1.97	4.04	2.13	2.91	3.40	1.53	3.58	0.67
Na_2O	3.18	3.57	2.98	2.68	3.49	4.01	4.45	3.86	2.82	3.49	2.60	2.74	1.94
K_2O	3.39	3.94	3.98	5.62	3.25	2.69	3.69	5.17	1.78	3.25	5.36	4.38	4.29
TiO_2	0.60	0.36	1.56	1.41	1.78	1.15	1.03	1.60	1.95	1.42	1.81	1.22	2.00
P_2O_5	0.20	0.14	0.23	0.10	0.37	0.09	0.08	0.28	0.19	0.10	0.12	1.36	0.09
L.O.I	2.62	3.38	3.22	3.25	6.45	4.35	2.16	3.86	5.81	7.93	3.62		
Ba	812	842	895	1531	260	725	1126	1724	603	1426	2954	1108	2390
Be	2.41	3.05	5.60	4.00	2.62	2.70	2.79	4.33	3.47	10.87	7.92	4.77	10.03
Cd	16.82	0.48	1.56	1.23	0.58	2.03	0.31	0.34	1.50	0.25	0.42	0.52	0.16
Ce	65.03	60.44	105.80	72.16	31.31	56.36	99.05	133.10	37.03	69.62	191.70	124.10	151.70
Co	21.44	4.16	19.09	11.74	29.04	24.20	16.83	14.15	16.92	13.27	19.60	25.04	18.59
Cr	25.10	16.86	143.90	149.50	57.32	84.55	90.22	142.90	112.0	100.90	160.90	91.68	167.20
Cs	2.71	2.37	7.23	3.07	10.52	2.72	3.70	9.43	2.66	12.86	6.98	6.82	6.36
Cu	17.77	9.41	6.00	8.78	6.27	18.66	18.26	0.00	40.17	14.38	7.84	7.01	5.82
Dy	3.37	3.15	5.54	2.90	2.94	2.57	3.25	7.07	3.00	2.32	7.70	15.10	9.02
Er	1.77	1.66	2.83	1.35	1.79	1.27	1.15	3.59	1.56	1.14	4.05	7.43	5.01
Eu	1.11	0.84	1.79	1.85	0.90	1.31	2.14	2.38	1.73	1.50	3.72	3.75	3.73
Ga	20.52	20.20	37.71	28.55	28.21	28.76	32.22	34.25	34.53	29.58	33.02	26.96	40.14
Gd	4.01	3.73	6.73	4.15	2.92	3.33	4.91	8.02	3.35	3.19	9.87	17.63	9.40
Ge	1.45	1.34	1.90	1.58	1.55	1.65	1.88	2.19	1.74	2.04	3.01	2.00	4.50
Hf	4.56	4.59	6.92	5.12	3.72	8.27	7.24	7.69	3.42	5.94	8.51	20.46	8.48
Ho	0.68	0.62	1.09	0.53	0.67	0.49	0.51	1.38	0.62	0.44	1.52	2.76	1.76
La	32.77	30.12	53.55	34.47	14.25	27.73	48.09	66.34	18.48	34.49	89.82	54.26	76.65
Lu	0.26	0.25	0.43	0.21	0.26	0.21	0.18	0.53	0.18	0.18	0.60	1.09	0.80
Mo	3.70	0.00	1.22	0.66	1.78	1.22	1.03	5.15	0.00	0.80	0.89	0.50	0.52
Nb	8.89	8.20	22.32	19.87	13.94	22.19	20.45	23.92	29.03	14.03	23.70	19.07	21.88
Nd	26.86	24.64	45.64	30.20	14.93	22.70	38.62	55.05	16.25	26.83	82.41	61.38	64.28
Ni	40.64	10.95	45.82	37.63	39.26	57.29	32.79	27.70	47.96	30.10	30.30	35.97	55.67
Pb	431.85	51.84	142.78	542.61	43.15	151.1	39.06	30.79	299.0	11.57	43.81	41.64	22.47
Pr	7.33	6.74	12.28	8.05	3.73	6.16	10.76	14.91	4.09	7.46	21.78	15.25	17.46
Rb	103.60	128.1	148.60	136.90	201.3	104.8	151.20	147.30	76.03	137.70	185.50	189.90	169.00
Sm	4.91	4.71	8.39	5.82	3.15	4.37	6.77	10.23	3.66	4.51	15.09	16.35	11.43
Sr	360.1	263.1	387.8	652.9	316.4	573.6	464.3	477.7	214.5	350.8	545.0	312.7	377.0
Ta	0.99	1.03	2.00	1.73	1.33	1.65	1.58	2.06	1.91	1.29	2.47	1.73	2.40
Tb	0.58	0.53	0.94	0.55	0.45	0.46	0.64	1.22	0.49	0.43	1.36	2.68	1.50
Th	13.07	15.44	15.88	10.89	5.13	16.30	20.07	21.83	6.03	7.89	24.65	18.77	22.16
U	6.51	5.88	3.16	4.18	3.19	4.79	3.46	4.03	4.10	2.58	4.00	5.81	3.62
V	62.05	32.99	204.1	192.9	162.2	99.54	124.8	205.2	182.6	156.3	216.8	140.5	234.0
W	1.59	0.41	2.94	4.91	2.94	2.65	1.40	22.49	2.17	1.94	1.62	2.74	1.66
Y	18.41	18.34	27.05	13.63	17.70	13.18	12.13	35.19	18.43	11.57	37.15	79.46	45.80
Yb	1.68	1.59	2.73	1.27	1.68	1.28	1.08	3.39	1.25	1.10	3.96	7.22	5.16
Zn	1636.0	73.21	776.1	348.7	154.4	260.1	257.6	339.2	440.3	123.3	120.6	200.4	244.0
Zr	174.20	160.10	246.60	179.00	154.80	299.50	255.40	287.10	129.60	224.20	307.10	685.50	301.50
ΣREE	529	487	873	570	305	451	735	1083	352	522	1495	1317	1297

Table 6

Non modal partial melting models

	Model 1 *Ma3*			**Model 2 *Ma5***		
Pressure *P* (kbar)	6			3		
Solidus temperature T_0 (°C)	738			810		
Peak temperature *T* (°C)	900			900		
Phase proportions (wt %)	**at T_0**	**in the melting assemblage**		**at T_0**	**in the melting assemblage**	
Bt	0.31	0.55		0.14	0.43	
Crd	0.00			0.14	0.21	
Pl	0.05	0.11		0.59	0.23	
Kfs	0.48			0.03		
Qz	0.10	0.23		0		
Sil	0.05	0.11		0		
Gt	0.02			0		
Sp	0.00			0.04		
Ilm	0.00			0.01		
Crn	0.00			0.06	0.13	
melt	0					
Final melt fraction (wt%)		**21**			**15**	
	D_{bulk}	***P***	***Cs/C₀***	D_{bulk}	***P***	***Cs/C₀***
La	0.72	0.54	0.94	2.78	1.08	1.11
Ce	0.61	0.46	0.90	2.34	0.91	1.10
Pr	0.64	0.51	0.91	2.55	1.01	1.11
Nd	0.40	0.33	0.78	1.55	0.63	1.07
Sm	0.30	0.19	0.71	0.89	0.38	1.00
Eu	1.27	0.36	1.07	1.85	0.70	1.08
Gd	0.52	0.28	0.88	1.29	0.57	1.05
Tb	1.26	0.42	1.07	1.92	0.94	1.08
Dy	2.11	0.31	1.14	1.33	0.72	1.05
Ho	3.69	0.29	1.18	1.34	0.82	1.05
Er	8.39	0.34	1.22	1.63	1.17	1.07
Tm	9.91	0.30	1.23	1.43	1.07	1.05
Yb	7.69	0.16	1.22	0.76	0.61	0.96
Lu	12.17	0.26	1.23	1.44	1.32	1.05
V	24.64	44.08	1.23	11.05	34.25	1.15
Cr	13.74	23.59	1.22	6.17	18.45	1.13
Ni	3.23	5.59	1.14	1.98	5.02	1.05
Nb	7.82	13.91	1.20	3.41	10.55	1.09